ESA CONTRACT REPORT

Contract Report to the European Space Agency

SMOS Continuous Monitoring Report - Part 1

Joaquín Muñoz Sabater,
Patricia de Rosnay, Mohamed Dahoui

ESA/ESRIN Contract 20244/07/I-LG

European Centre for Medium-Range Weather Forecasts
Europäisches Zentrum für mittelfristige Wettervorhersage
Centre européen pour les prévisions météorologiques à moyen terme

ECMWF

Series: ECMWF ESA Project Report Series

A full list of ECMWF Publications can be found on our web site under:
http://www.ecmwf.int/publications/

Contact: library@ecmwf.int

European Centre for Medium Range Weather Forecasts
Shinfield Park, Reading, RG2 9AX, England

Contract Report to the European Space Agency

SMOS Continuous Monitoring Report - Part 1

Authors: Joaquín Muñoz Sabater,
Patricia de Rosnay, Mohamed Dahoui
Continuous Monitoring Report - Part 1
ESA/ESRIN Contract 20244/07/I-LG

European Centre for Medium-Range Weather Forecasts
Shinfield Park, Reading, Berkshire, UK

February 2011

	Name	Company
First version prepared by (December 2010)	J. Muñoz Sabater	ECMWF
Quality Visa	E. Källén	ECMWF
Application Authorized by	N. Wright	ESA/ESRIN

Distribution list:

ESA/ESRIN
Luc Govaert
Susanne Mecklenburg
Steven Delwart
Norrie Wright
ESA ESRIN Documentation Desk

SERCO
Raffaele Crapolicchio

ESA/ESTEC
Catherine Bouzinac
Matthias Drusch

ECMWF
HR
Division & Section Heads

Abstract

Contracted by the European Space Agency (ESA), the European Centre for Medium-Range Weather Forecasts (ECMWF) is involved in global monitoring and data assimilation of the Soil Moisture and Ocean Salinity (SMOS) mission data. For the first time, a new innovative remote sensing technique based on radiometric aperture synthesis is used in SMOS to observe soil moisture over continental surfaces and ocean salinity over oceans. Monitoring SMOS data (i.e. the comparison between the observed value and the model equivalent of that observation) is therefore of special interest and a requirement prior to assimilation experiments. This report is the first part of a series of Monitoring Reports of the ESA Request for Quotation RfQ 3-11640/06/I-LG. The objective is to report on the monitoring activities of SMOS data over land and sea on a long term basis, exploiting also the multi-angular and multi-polarised aspect of the SMOS observations. Some of the first results obtained are shown in this report. Some case studies have also demonstrated the ability of SMOS data to observe soil moisture in all weather conditions.

1 Introduction

ECMWF has developed an operational chain which is able to monitor SMOS data in Near Real Time (NRT) at global scale, as explained in (Sabater et al. 2010a). Monitoring is carried out routinely for each new type of satellite data brought into the operational Integrated Forecasting System (IFS) at ECMWF. Although there are different definitions of monitoring, in Numerical Weather Prediction systems monitoring is mainly the comparison between the observed variable and the model equivalent simulating that observation, because this is the quantity used in the analysis.

For SMOS, monitoring is produced separately for land and oceans. The reason is the strong contrast between the dielectric constant of water bodies and land surfaces, which in turn produce very different emissivities and observed brightness temperatures at the top of the atmosphere. Thus, monitoring SMOS data separately over land and oceans increases the sensitivity to the statistical variables. Moreover, the multi-angular and multi-polarised aspect of the observations is also accounted for in the monitoring chain by monitoring the data independently for several incidence angles of the observations and for two polarisation states at the antenna reference frame.

The developed framework makes it possible to obtain daily statistics of the observations, the model equivalent of the observations computed by the Community Microwave Emission Model (CMEM) [(Drusch et al. 2009; de Rosnay et al. 2009a)], and the difference between both sources of information, the so called first-guess departures. The statistical method uses several weeks of data. This is a very robust way to identify systematic differences between modelled values and observations. Furthermore it also set the basis to investigate and understand the new observations before they become active in the ECMWF land assimilation scheme.

This first Monitoring Report (MR1) on SMOS data has two main objectives:

- To describe the statistical products obtained in routine mode as part of the SMOS monitoring chain in research mode [see (Sabater et al. 2010a)].
- To demonstrate the potential of SMOS observations to monitor soil moisture under all weather conditions, but also of other surface variables sensitive to L-band.

2 SMOS observations at ECMWF

SMOS Near Real Time (NRT) products are processed at the European Space Astronomy Centre (ESAC) in Madrid (Spain) and sent to ECMWF via the SMOS Data Processing Ground Segment (DPGS) interface. The product used at ECMWF is the NRT product which are geographically sorted swath-based maps of brightness temperatures. The geolocated product received at ECMWF is arranged in an equal area grid system called ISEA 4H9 (Icosahedron Snyder Equal Area grid with Aperture 4 at resolution 9) [see (Matos and Gutierrez 2004)]. For this grid, the centre of the cell grids are at equal distance of 15 km over land, with a standard deviation of 0.9 km. For the NRT product, the resolution is coarser over oceans as they present lower heterogeneities that continental surfaces. The format of the NRT product is the Binary Universal Form for the Representation of meteorological data (BUFR). Each message in BUFR format corresponds to a snapshot where the integration time is 1.2 seconds. In average, each snapshot contains around 4800 subsets over land.

3 Simulations of brightness temperatures in L-band

In order to simulate brightness temperatures at L-band and compare them to the SMOS observations, ECMWF has developed the Community Microwave Emission Model (CMEM). It constitutes the forward model operator for low frequency passive microwave brightness temperatures of the surface. Although for SMOS purposes it is used at 1.4 GHz, potentially it can be used up to 20 GHz. This software package is fully coded in Fortran-90 language. It has been designed to be highly modular providing a good range of I/O interfaces for the Numerical Weather Prediction Community. CMEM surface forcing comes from the integration of the operational H-TESSEL (Hydrology Tiled ECMWF Scheme for Surface Exchanges over Land) land surface scheme [(Balsamo et al. 2009)]. H-TESSEL is forced with meteorological fields of surface pressure, specific humidity, air temperature and wind speed at the lowest atmospheric level. The surface radiation and precipitation flux represent 3-h averages, and they are kept constant over a 3-h period. The integration of HTESSEL provides the soil moisture and soil temperature fields, as well as snow depth and snow density fields, which are then coupled with CMEM to simulate ECMWF first-guess L-band brightness temperatures. Additional land surface information needed is soil texture data obtained from the Food and Agriculture Organization (FAO) data set, whereas sand and clay fractions have been computed from a lookup table according to (Salgado 1999). The soil roughness standard deviation of height (σ) parameter in CMEM is set to 2.2 cm as in (Holmes et al. 2008). Vegetation type is derived from the H-TESSEL clasification, whereas a MODIS climatology is used to derive leaf area index (LAI).

CMEM's physics is based on the parameterizations used in the L-Band Microwave Emission of the Biosphere [LMEB, (Wigneron et al. 2007)] and Land Surface Microwave Emission Model [LSMEM, (Drusch et al. 2001)]. The modular architecture of CMEM makes it possible to consider different parameterizations of the soil dielectric constant, the effective temperature, the roughness effect of the soil and the vegetation and atmospheric contribution opacity models. In the current configuration of CMEM, the vegetation opacity model of (Kirdyashev et al. 1979) is used, in combination with the (Wang and Schmugge 1980) dielectric model, the (Wigneron et al. 2001) effective temperature model and the simple soil roughness model of (Choudhury et al. 1979). The atmospheric contribution is accounted for as in (Pellarin et al. 2003). This combination of parameterizations were shown to be well suited for brightness temperature modelling (Drusch et al. 2009; de Rosnay et al. 2009a; Sabater et al. 2010b). However these results are based on local and regional scale experiments and a global sensitivity study has not yet been undertaken.

Note also that CMEM is a SMOS Validation and Retrieval Teams (SVRT) tool freely available at *http://www.ecmwf.int/research/ESA_projects/SMOS/cmem/cmem_index.html*. More information about CMEM can be found in (de Rosnay et al. 2009b).

4 Statistical products

The main output of the monitoring chain developed at ECMWF is the routine production of statistics about SMOS data and the simulation of SMOS data in NRT. In part III of (Sabater et al. 2010a) a detailed list of these statistical products can be found. In particular, spatio-temporal averages of the SMOS observed brightness temperatures, the modelled brightness temperatures and the first guess departures, as well as of their standard deviation, are computed. These statistics and plots are updated once per day and include data for a period of about seven weeks. They are published and available in NRT via the ECMWF SMOS website: *http://www.ecmwf.int/research/ESA_projects/SMOS/monitoring/smos_monitor.html*. In Fig. 1 an overview of the statistical products which are currently obtained in NRT (and possibly during all the SMOS lifetime) with the offline monitoring chain is shown. For each product obtained, statistical variables can be selected independently for land and sea surfaces and for the XX and YY polarisations states in the satellite antenna reference frame. Also, six different incidence angles, from 10 to 60 in multiples of 10 plus an offset of 0.5 degrees around these angles, can be monitored independently. Therefore, each day at least 24 figures are produced and updated per statistical variable and product. The three main groups of products are the following:

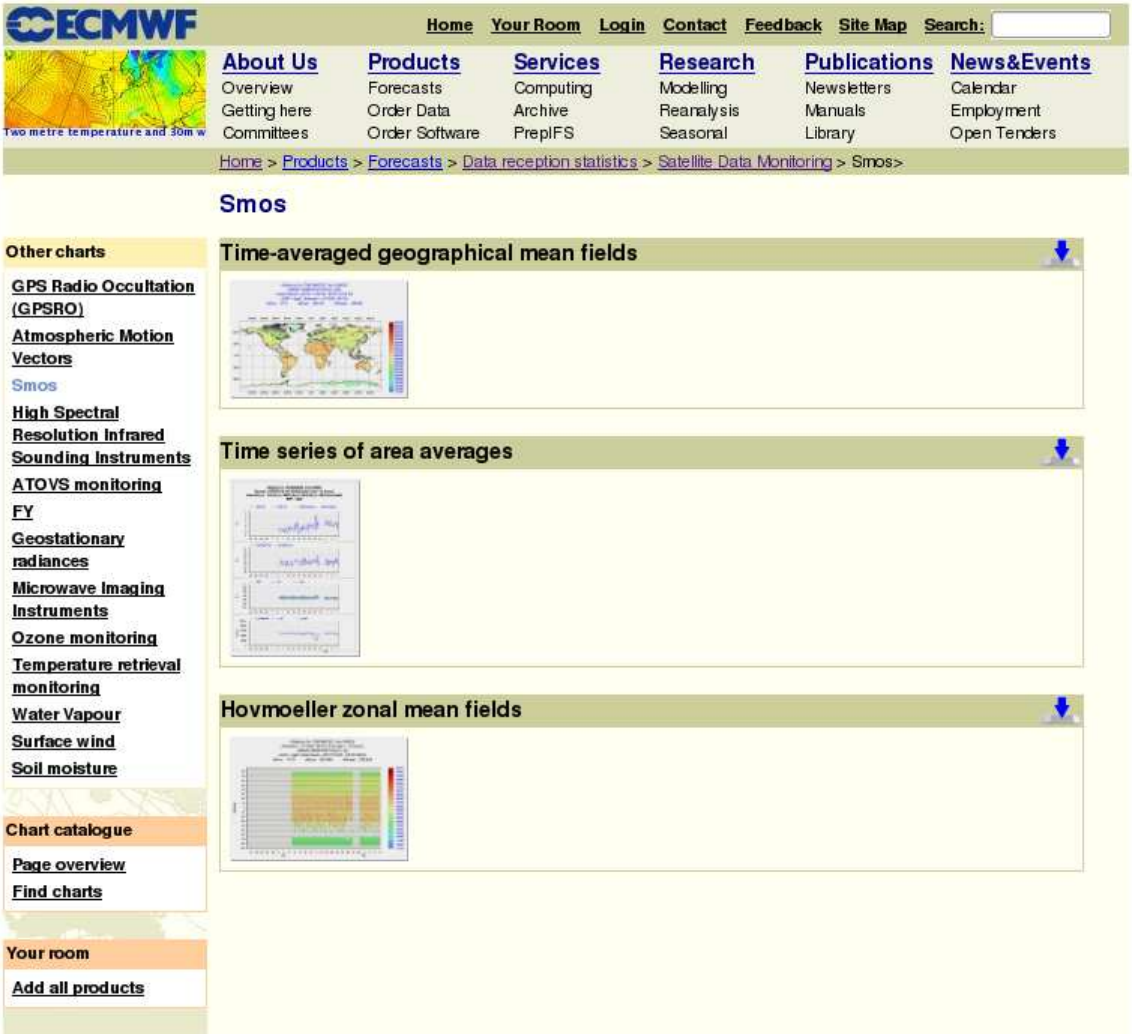

Figure 1: Overview of statistical products obtained with the SMOS monitoring chain. Visit http://www.ecmwf.int/research/ESA_projects/SMOS/monitoring/smos_monitor.html.

1. **Time-averaged geographical mean field**: these plots provide a time-averaged mean value for the observed brightness temperatures and the first guess departures, as well of their standard deviation. They average all the values contained in a grid box of pre-defined resolution from a period of at least seven weeks. These plots are useful to localize areas where Radio Frequency Interference is strong, but also they show significant correlations with physical land variables. Fig 2 shows an example of these plots for the whole month of June 2010. It corresponds to averaged values of the observations at 50 degrees incidence angle and at the XX polarisation state.

2. **Time series of area averages**: their main purpose is to obtain time series of the observed brightness temperatures and the first guess departures. Values shown represent one mean value per 12 hours assimilation cycle averaged at global scale. By default these plots will produce statistics for the last seven weeks of data.

3. **Hovmöller zonal mean fields**: these plots have as objective to plot one mean value averaged per predefined bands of latitude as a function of time. They provide a latitudinal-temporal perspective of the produced statistical variables and thus they make it possible to analyse the seasonal evolution of average values per bands of latitude. Punctual problems in the data that could be unnoticed in time-averaged geographical plots, can be easy localized in this format.

A set of updates for these statistics is planned for the next ECMWF cycle 37r1 (early in 2011), where a new statistical product depicting first-guess departures as a function of the incidence angle, averaged per grid box and containing several weeks of data, will be included too. Additionally and in order to support cal/val teams, statistics will also be produced independently for a serie of targeted areas which are detailed here below:

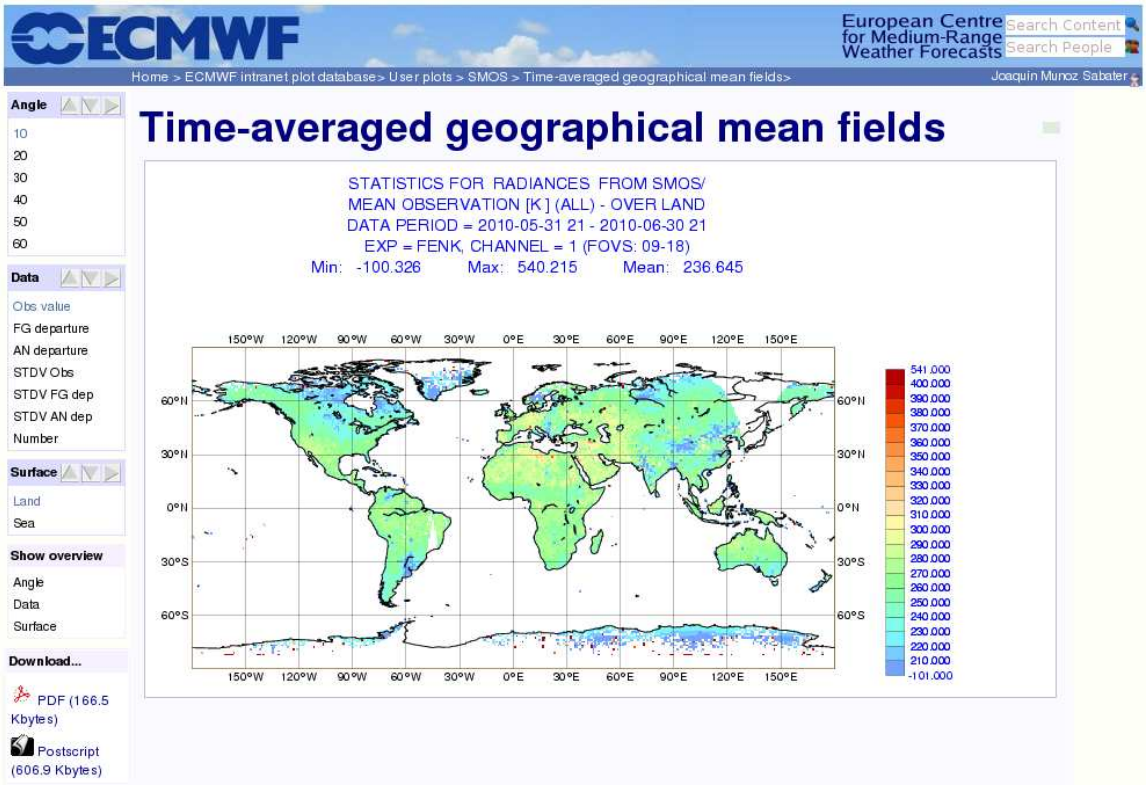

Figure 2: Example of statistical products obtained with the SMOS monitoring chain. This figure represents the averaged value of the observed brightness temperatures at 10 degrees incidence angle over continental surfaces.

1. Continental areas: North Hemisphere, South Hemisphere, Europe, Asia, NorthAmerica, SouthAmerica and Australia (only for continental surfaces),
2. Sites from the Soil Climate Analysis Network (SCAN) of United States:
   - Lancaster : lat. 40.89 N, lon. -96.50 W,
   - Chase : lat. 40.38 N, lon. -101.75 W,
   - Nemaha; : lat. 39.70 N, lon. -96.16 W,
   - Darlington : lat. 34.30 N, lon. -79.73 W,
   - Little River : lat. 31.50 N, lon. -83.50 W (covering an area of 1.25x1.25 degrees),
   - Little Washita : lat. 34.90 N, lon. -98.00 W (covering an area of 1.25x1.25 degrees),
   - Reynolds Creek : lat. 43.10 N, lon. -116.8 W (covering an area of 1.25x1.25 degrees),
3. Dome-C site in Antarctica: lat. -75.128 S, lon. 123.42 (covering an area of 0.5x0.5 degrees),
4. Australian Airborne Cal/Val Experiment (AACES) site in Australia: the area covered is lat. [-35.5 S, -34 S], lon. [143 E, 149.5 E],
5. Niamey area (Niger); area covered is lat. [13 N, 14 N], lon. [1.6 E, 3 E],
6. Loueme watershed (Benin): the area covered is lat. [9 N, 10.2 N], lon. [1.5 E, 2.8 E],
7. Sodankylae in Finland, covering one degree box from lat. [67 N, 68 N], lon. [26 E, 27 E],
8. HOBE site in Denmark; lat. 55.96 N, lon. 9.13 E,
9. SMOSREX in France: lat. 43.42 N, lon. 1.33 E,
10. The Valencia Anchor Station (VAS) in Spain; are covered is lat. [39.22 N, 39.68 N], lon. [1.11 W, 1.70 W],
11. Upper Danube catchment: area covered is lat. [46.2 N, 50.2 N], lon. [7.9 E, 14.0 E],
12. SMOSmania network in France: covering an area of 3.4x5.8, centered on lat. 44.03 N, lon. 1.03 E.

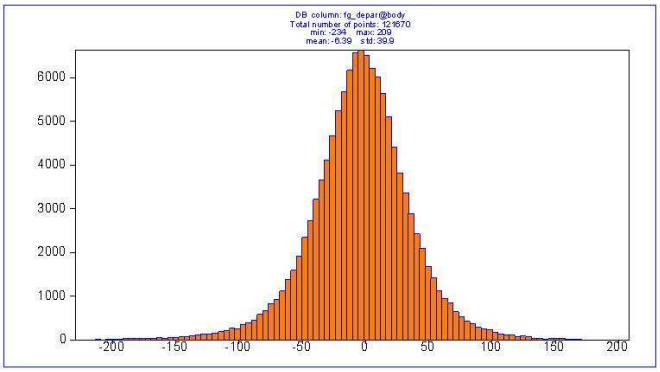

(a) XX polarisation mode

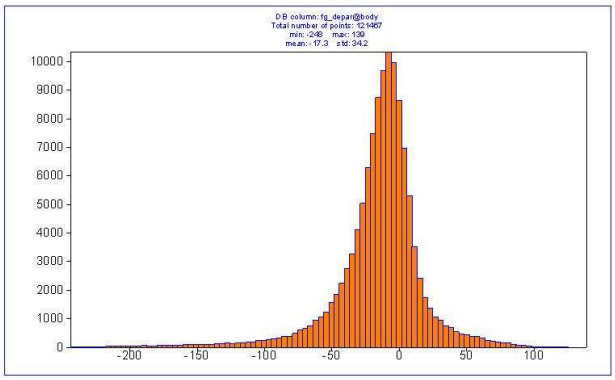

(b) YY polarisation mode

Figure 3: Histogram of first-guess departures between SMOS observations and CMEM simulations for the 00Z ECMWF 4DVAR 12 h cycle on the 22nd of January 2010.

5 Analysis of the main reasons for large departures

In the context of Numerical Weather Prediction (NWP) observed radiances are compared to their modelled equivalent computed with a radiative transfer model, with the aim of producing first-guess departures. This is the main entity which feeds the assimilation schemes. If significant departures are found between observations and simulations then it is important to understand what is causing these large departures. This is useful in views of the design of a bias correction scheme, but also because decisions concerning which data will be assimilated have to be done. In this section two case studies are presented to investigate the main reasons for large departures between SMOS observations and simulated brightness temperatures.

The first case study investigates data for the 22nd of January 2010, almost three months after the launch of the SMOS satellite. The data used in this case study corresponds to the 00Z 12 hours cycle of the ECMWF 4DVAR atmospheric analysis and thus contains data acquired from 21h00 on the 21st of January 2010 to 9h00 on the 22nd of January 2010. No filtering per incidence angle or geographical area was carried out. Figs. 3a and Fig. 3b shows the probability distribution functions of the first-guess departures for this case study. The histograms show functions which have the shape of normal distributions with mean close to zero. This first result is very positive as firstly it means that in average CMEM is simulating with accuracy brightness temperatures at the top of the atmosphere in L-band (taken as reference SMOS observations) and secondly, the relatively small average mean bias shows that most of the simulations over individual pixels were computed accurately too. However the probability distribution functions have long tails at both sides of the mean value, suggesting that a significant number of large differences between model and observations are present.

Fig. 4 shows the geographical distribution of first-guess departures larger than 75 K for this case study, which is a very large value. It is observed that almost all the data within this category corresponds to overpasses in Europe and Asia. These areas have already been identified as areas strongly affected by RFI, at least for the date of this case study. However, Fig. 5 shows the orography for these locations. Areas with high latitude, as the Tibet plateau and the Alps mountains in Europe show the largest departures. This result suggests that a combination of the altitude, the slope, ice and snow is one of the main reasons to obtain large positive departures. This result is somehow expected, as the capabilities of the microwave forward modelling for these areas is currently very inaccurate. Although for monitoring purposes is very interesting to pinpoint these large departures, assimilation experiments will mask these areas beforehand.

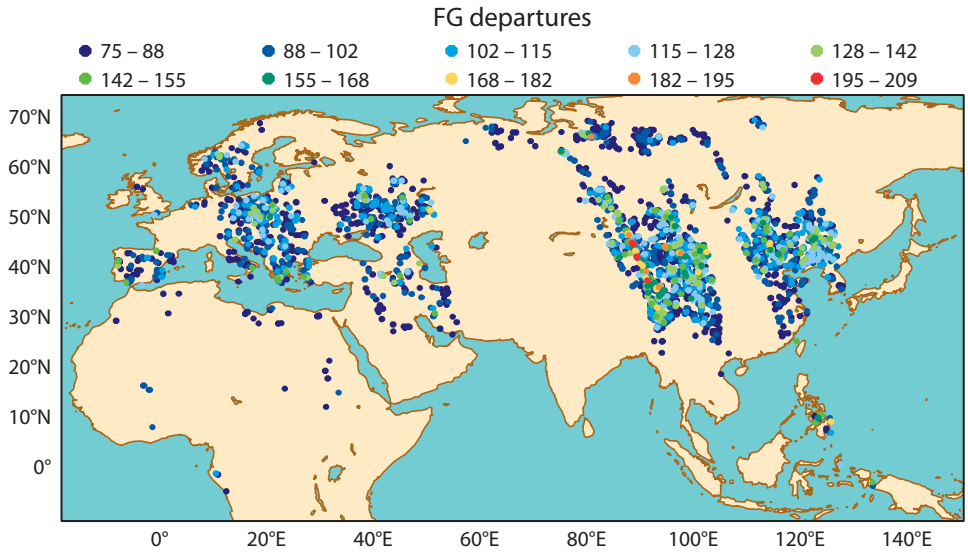

Figure 4: Geographical location and value of first-guess departures larger than 75 K. Observations used in this plot correspond to the 00Z ECMWF 4DVAR 12 h cycle on the 22nd of January 2010.

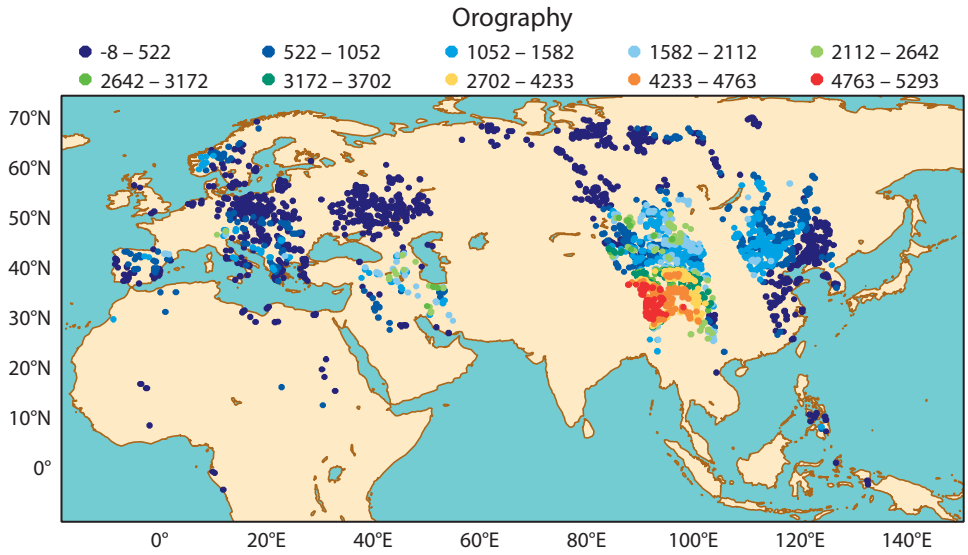

Figure 5: Orography of first-guess departures geographical locations larger than 75 K. Observations used in this plot correspond to the 00Z ECMWF 4DVAR 12 h cycle on the 22nd of January 2010. Altitude values are in meters.

In Fig. 6 the location and value of the most negative departures (lower than -100 K), i.e, when the observations are strongly overestimated by the simulations, is found to be for Australia and Indonesia. Strong negative departures are found in Europe, Asia and North of Africa too, just as it was the case for the large positive departures group. The main cause is again RFI. RFI does not necessarily has as effect increasing the brightness temperatures. However it depolarises the signal and therefore it can also decrease the intensity of the geophysical signal.

Strong negative departures are found near coastlines. Fig. 6 shows the location and value of these large departures for Australia. The coastline effect is due to strong differences in brightness temperatures over land and sea. If the model grid point is over land, eventually the simulated brightness temperature will be much larger than the SMOS observation if the nearest observation is over sea or if the re-sampled observation in the ISEA

grid accounts also for sea contribution. It is also observed that some of these very large negative departures occurs in the interior of Australia. In Fig. 7 the incidence angle corresponding to the observations displayed in Fig. 6 is shown too. Most of the incidence angles are around 60 degrees. This result suggests that modelled brightness temperatures can be strongly overestimated for very dry areas under large incidence angles. It is well known that roughness effects are not well modelled yet for large incidence angles in L-band, and in particular for the horizontal polarisation. Dry conditions increase soil roughness and the influence of this effect under large incidence angles is not yet well accounted for in the current soil roughness parameterization of CMEM.

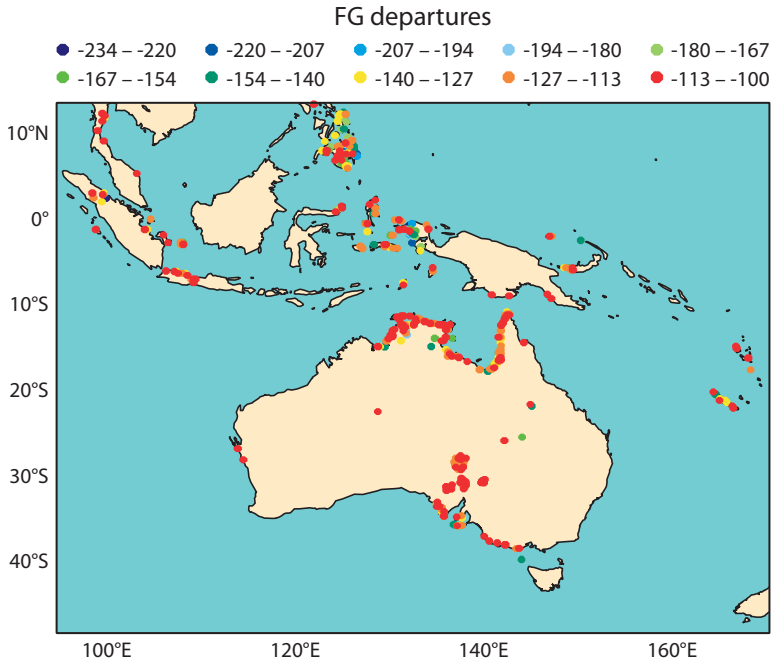

Figure 6: Geographical location and value of first-guess departures lower than -100 K. Observations used in this plot correspond to the 00Z ECMWF 4DVAR 12 h cycle on the 22nd of January 2010.

Fig. 8 shows the location and value of departures which are expected to present significant correlation with geophysical land variables for the YY polarisation. The maximum difference permitted between SMOS observations and modelled values was fixed to 25 K in absolute value. Complex patterns of departures are observed, which certainly show some correlation with the soil moisture state. In particular red dots (corresponding to departures between 20K and 25K) are quite well correlated with snow covered areas and boreal forests. Contrarily, over dry and desert areas blue dots (departures between -15K and -25K) are more predominant. These results suggest that CMEM underestimates observed radiances in L-band over snow and ice covered areas, as well as over boreal forests. Ice covered surfaces behave as if they are drier and therefore warmer in terms of brightness temperatures. This aspect is not yet well modelled by CMEM. However where roughness effects are very important CMEM's current parameterization overestimates the soil emission, in particular for large incidence angles.

The second case study investigates more recent data. It uses data for the 1st of October 2010. The orbits used are shown in Fig. 9a. Observations without geophysical meaning (lower than 50 K or greater than 350 K) are filtered out in previous steps. In this case only 6 different incidence angles are selected in order to reduce the processing burden of the data set. The selected angles are 10, 20, 30, 40, 50 and 60 (+/- an offset of 0.5). In terms of a snapshot this means that only several 'rings' within the field of view would be accounted for, as displayed in Figs. 9b. Fig. 10a and Fig. 10b show the histograms of brightness temperatures for the XX and YY polarisation states (as seen in the satellite antenna reference frame). Compared to Figs. 3a and 3b it can

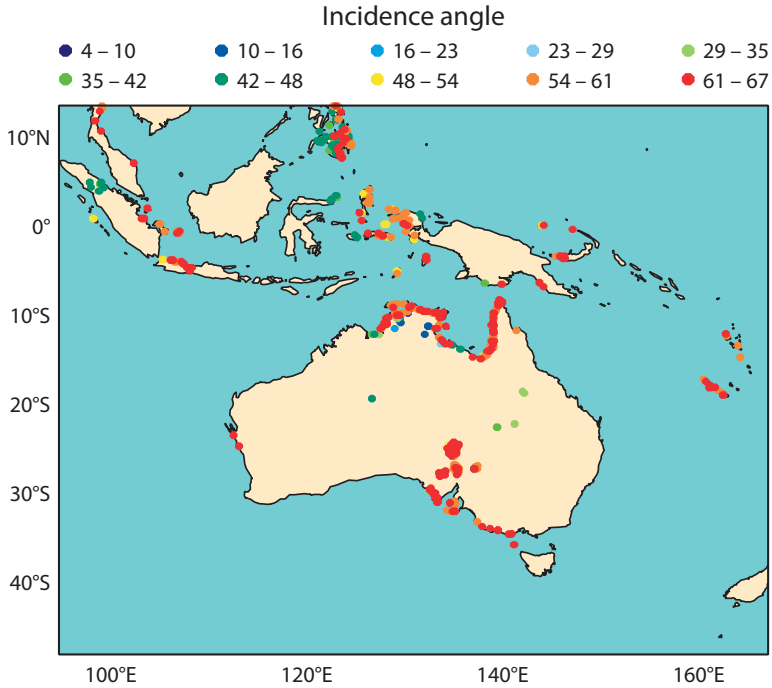

Figure 7: Incidence angle of the SMOS observations presenting first-guess departures lower -100 K in Australia. Observations used in this plot correspond to the 00Z ECMWF 4DVAR 12 h cycle on the 22nd of January 2010.

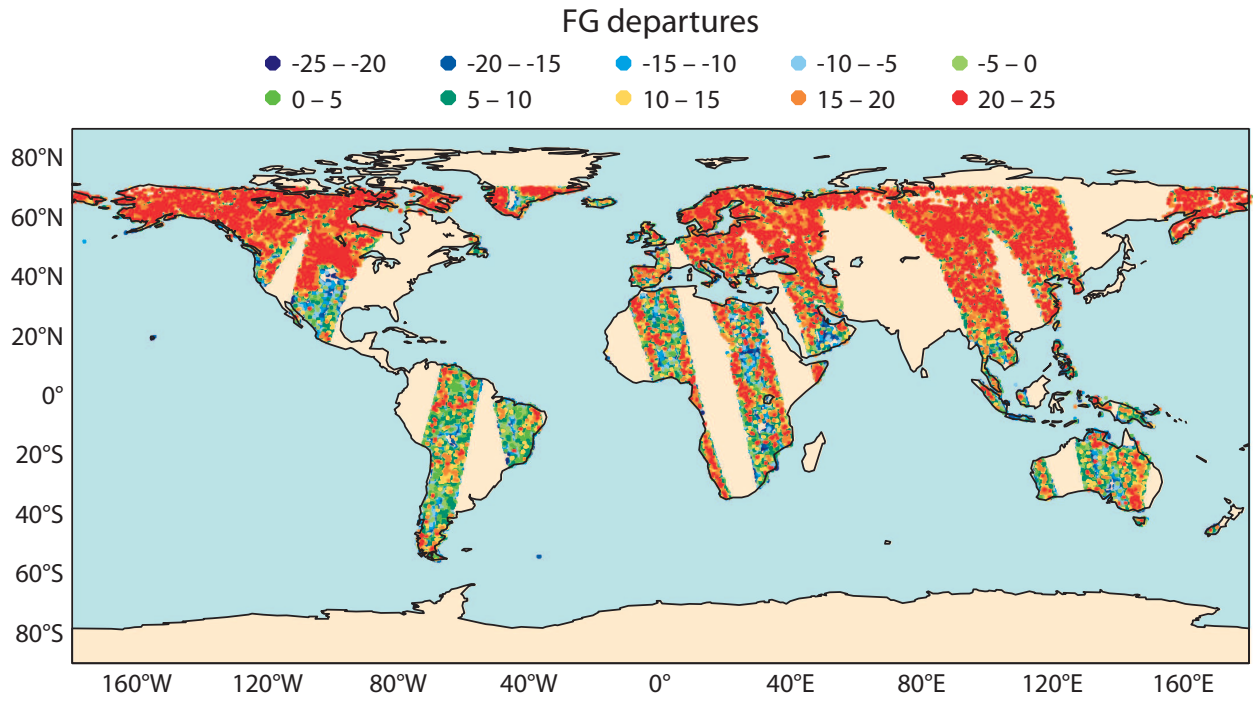

Figure 8: Geographical location and first-guess departure between -25 K and 25 K.

be observed that the shape of the histograms is relatively similar. However it can also be observed that the tails have decreased significantly for both distributions. There are several reasons for this improvement; first of all the instrument on-board of the SMOS satellite was calibrated several times since the beginning of the mission, which had also improved the quality of the reconstructed image. Secondly, there has been an intense fight

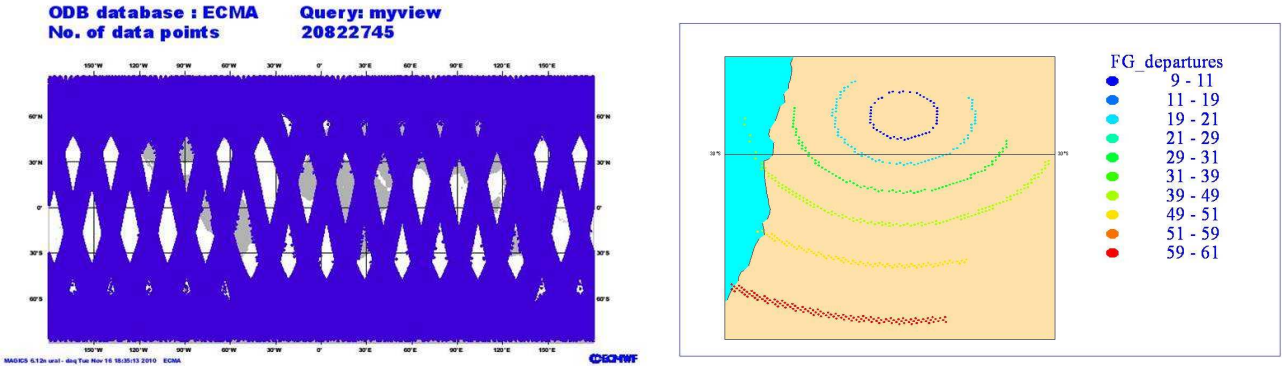

(a) (b)

Figure 9: (a) Orbits covered by the SMOS satellite the 1st of October 2010. (b) Location of different incidence angles in the field of view of a SMOS snapshot.

against illegal emission in L-band, which also has decreased the number of pixels affected by RFI. And thirdly, the inputs which feed the forward operator have improved from the ECMWF cycle 36r1 to the cycle used in this case study (cycle 36r4). In particular a better representation of the soil water content stored in the first seven cms of the soil is observed for bare soil areas. Figs. 11 and Figs. 12 show the soil moisture for the first 7 cm the 6th of October 2010 using the physics within the ECMWF cycle 36r3 and the cycle 36r4, respectively. It is observed a strong difference in all desert areas. The main raison for this difference is the introduction in the cycle 36r4 of a new improved bare soil evaporation scheme which allows to evaporate water below the wilting point in areas with sparse vegetation, thus producing more realistic dry values of the soil water content in these zones. This has demonstrated to have a direct and strong impact in the simulated brightness temperatures, as can be observed in Fig. 13. This figure shows the mean difference in simulated brightness temperatures in L-band over the month of August 2010, by using the physics in cycle 36r2 and cycle 36r4 and the current configuration of CMEM (see section 3). It can be seen that all bare soil areas are very affected by this change (up to 100 K). The global averaged difference between both cycles for the horizontal polarisation and the month of August is 6.5 K in contrast to 4.1 K for the vertical polarisation, which is less sensitive to changes in soil moisture. This improvement in the characterization of soil moisture of the first cms of the soil layer has a direct and significant impact on the simulated brightness temperatures and hence in the first-guess departures.

The histogram breakdown by incidence angles does not reveal new significant characteristics. In Fig. 14 the histograms of departures per incidence angle is shown for the XX polarisation. In general the distribution function of the histogram is maintained quite stable, but with a constant mean shifted towards negative departures with increasing the incidence angle. The situation is quite similar for the YY polarisation but with opposite sign, i.e., mean bias decreases with increasing the incidence angle.

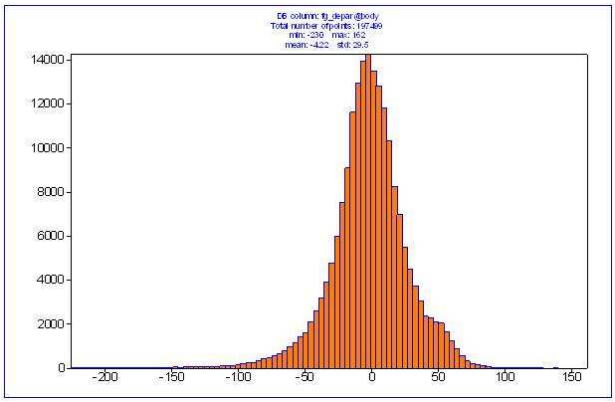

(a) XX polarisation mode.

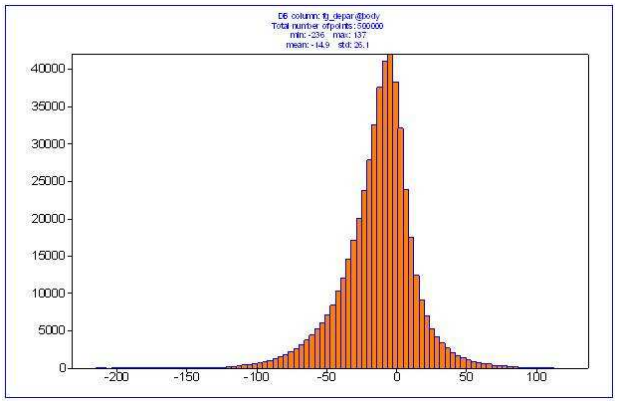

(b) YY polarisation mode.

Figure 10: Histograms of first-guess departures between SMOS observations and CMEM simulations for the 1st of October 2010 and for the XX and YY polarisation modes in the antenna reference frame.

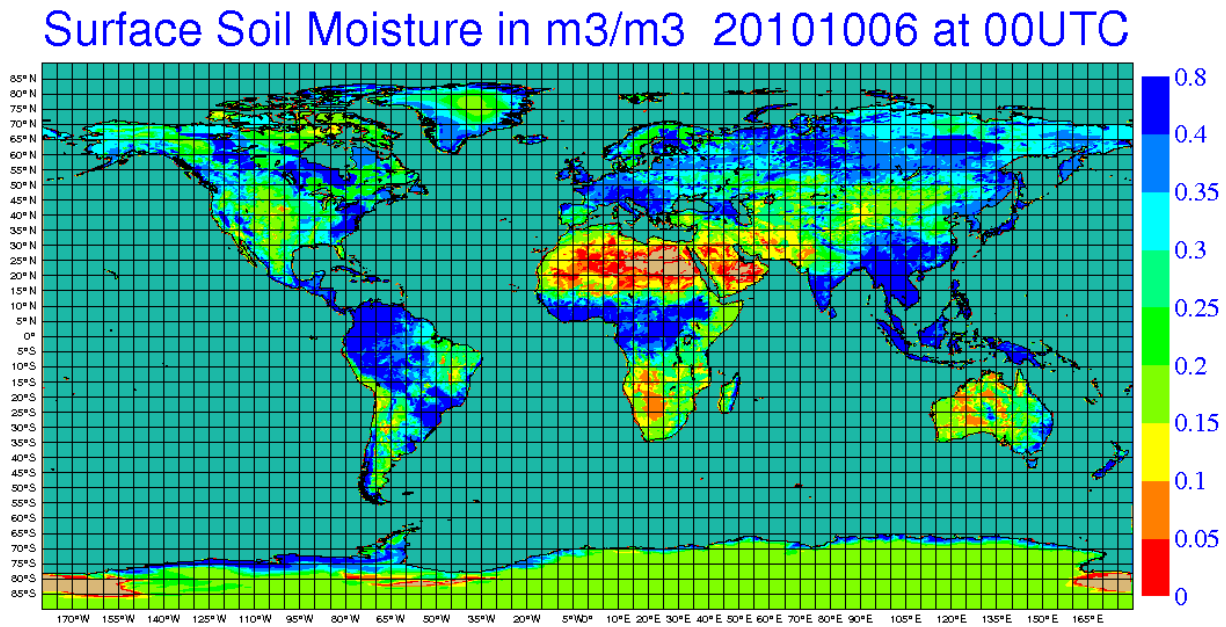

Figure 11: Soil moisture of the first 7 cm for 6th of October 2010 using physics in ECMWF cycle 36r2. Values are displayed in mm.

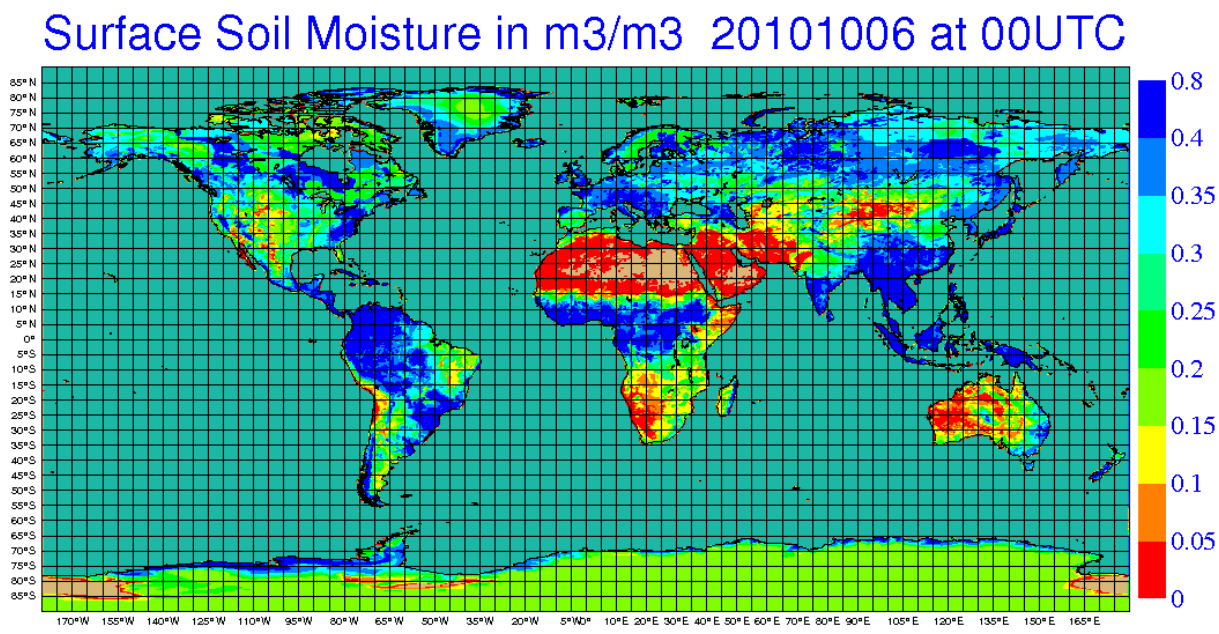

Figure 12: Similar to Fig. 11, but for ECMWF cycle 36r4.

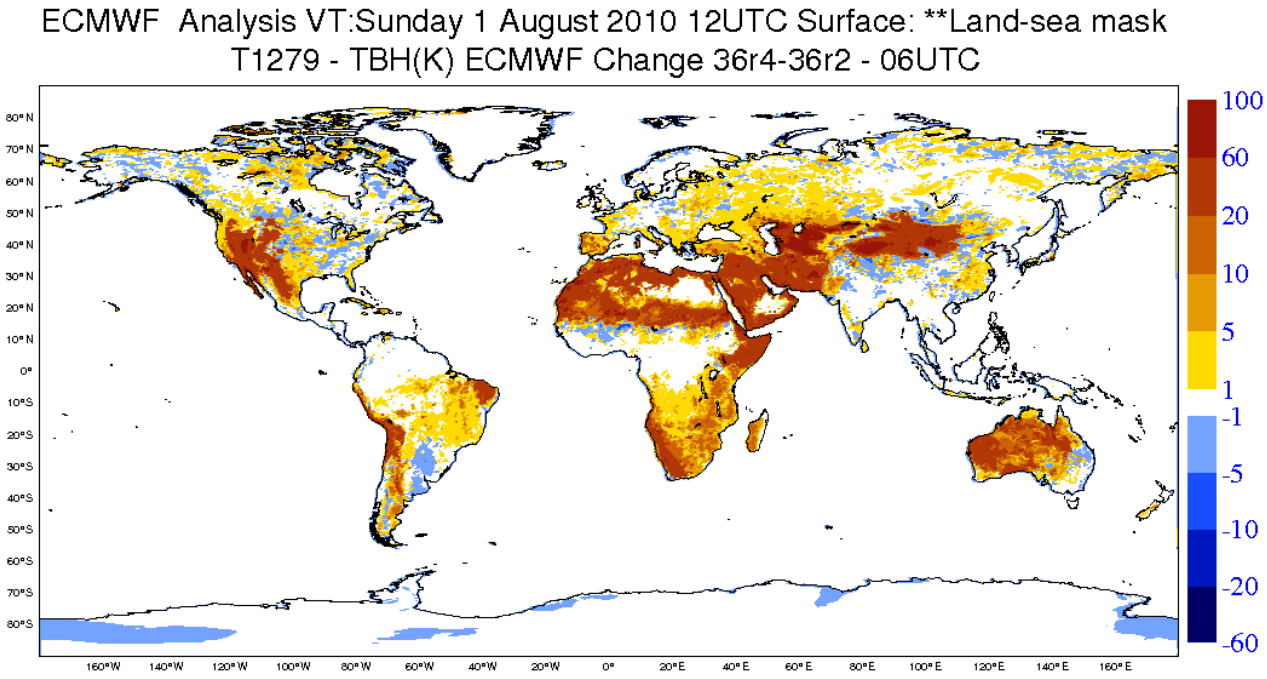

Figure 13: Sensitivity of soil moisture of the first seven cms of the soil to the modifications of physics from IFS cycles 36r2 to 36r4.

With the information gathered in the previous analysis, histograms of first-guess departures have been mapped to the main reasons of bias, as shown in Fig. 15. This figure makes it clear that RFI plays a very significant role in the large differences between observations and simulations, but it is not the only cause. Coastlines, mountainous areas, snow, ice and very dry zones at high incidence angles seem also to cause strong departures. For assimilation experiments, these areas will have to be blacklisted.

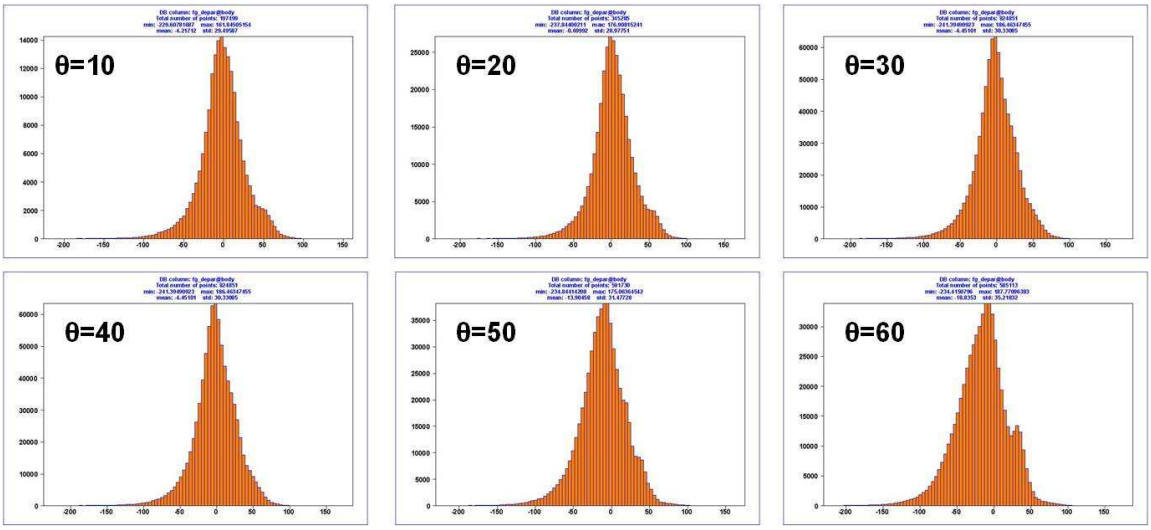

Figure 14: Histogram of first-guess departures between SMOS observations and modelled brightness temperatures for different incidence angles, for the 1st of October 2010 and XX polarisation.

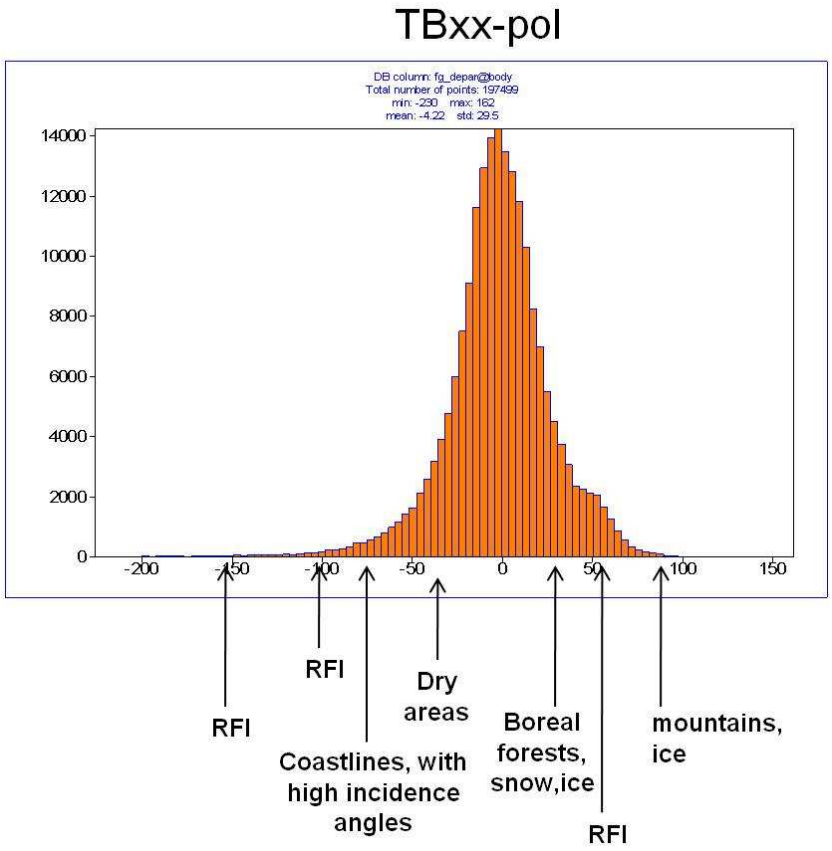

Figure 15: Main reasons for first-guess departures for the XX polarisation state.

6 Average observed values

Fig. 16 shows the temporal mean of the SMOS observed brightness temperatures as seen by the instrument for the first week of June 2010 at 0.25 degrees spatial resolution and an incidence angle of 40 degrees. This figure shows complex patterns which reflect the state of the soil (soil water content, soil temperature, roughness length, etc.) at the time of the observations. It has been checked that these values get colder with increasing the incidence angle for the XX polarisation, whereas the opposite happens for the YY polarisation, as theoretically should be expected. However brightness temperatures appear to be too high in this figure, as well as it happens for other incidence angles, in Europe, whereas too low values are registered in China. The effect of RFI is clear in these areas.

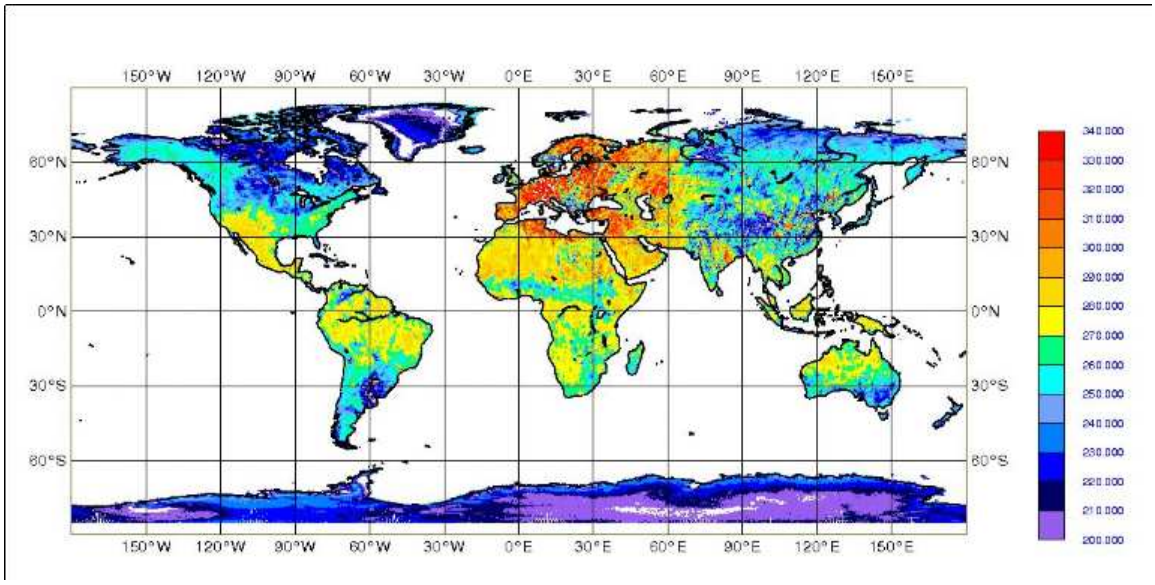

Figure 16: Average value of the SMOS brightness temperatures for the first week of June 2010, at 0.25 degrees spatial resolution and for the XX polarisation state.

Monitoring is also being done independently for oceans. Fig. 17 shows the average brightness temperature in grid-boxes of 1 degree from the 5^{th} to the 19^{th} of November 2010 for observations with an incidence angle of 40 degrees and for the YY polarisation. This figure shows that in average the polar latitudes are much warmer in terms of brightness temperatures than the rest of the oceans. This is the combination of several factors: firstly the water in these zones is colder and more fresh with lower salinity, factors which have an influence over the water emission in L-band, but the main reason is due to the ice in the poles. Over ice covered areas the soil behaves as it was drier which has a substantial warm effect on the brightness temperatures. In Fig. 18 the ECMWF sea ice cover analysis the 15^{th} of November 2010 is shown. It can be observed a very good correlation between both maps, what confirms the ability of SMOS data to monitor sea ice too.

7 First-guess departures

In this section a few examples of time-averaged geographical mean fields is given. Figs. 19, 20 and 21 represent the mean field of first-guess departures at global scale for the first week of March, April and May 2010 respectively. All the observations found within grid-boxes of 1 degree are averaged. These three figures show clearly the melting season of the snow at the North-Hemisphere. During the first week of March 2010 an extended area of the North Hemisphere is still covered by snow, what produced warm departures up to 27 K in vast areas. This

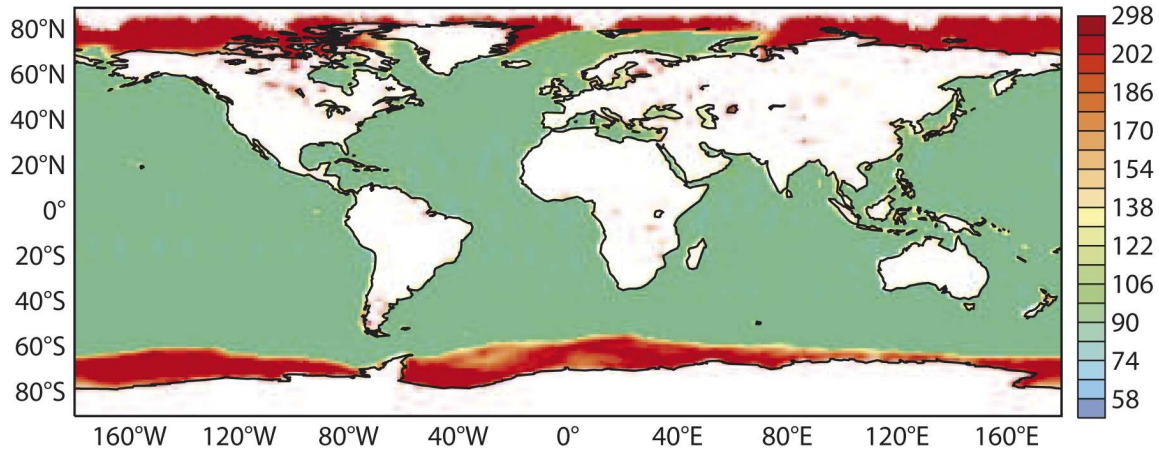

Figure 17: Average of the SMOS brightness temperatures over oceans at 1 degree spatial resolution from the 5th to the 19th of November 2010 at 40 degrees incidence angle and for the YY polarisation mode.

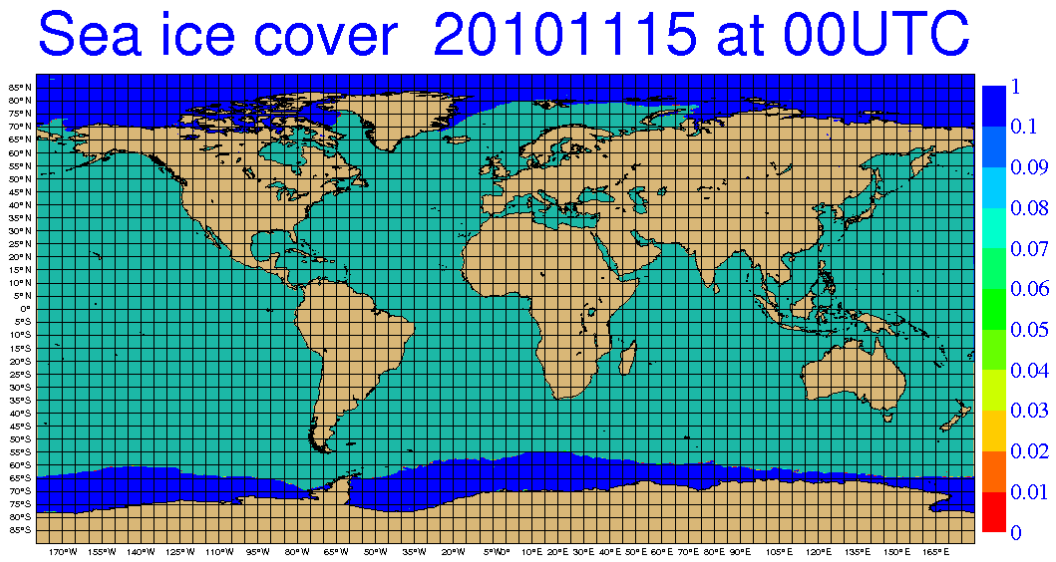

Figure 18: Analysed sea ice cover for the 15th of November 2010.

result was expected, as currently the passive microwave emission modelling does not represent ice and snow covered areas properly. With the melting in April this area moves progressively towards northern latitudes and it gets much smaller in May. Note also that the South Pole (with its permanent snow and ice cover) always displays red-yellow colours corresponding to high departures. The high values of first-guess departures found in the Himalayas are evident, but less visible for the course resolution of these statistics. It can also be seen at the European Alps. Strong negative departures are found in China, more related to RFI contamination. Dry areas show lower negative departures, which is consistent with the findings of the previous section.

8 Standard deviation of observations and first-guess departures

Computing geographical time-averaged standard deviation of the SMOS observations provide a good overview of the spatial variability of these observations during a given period. Given the strong sensitivity of brightness

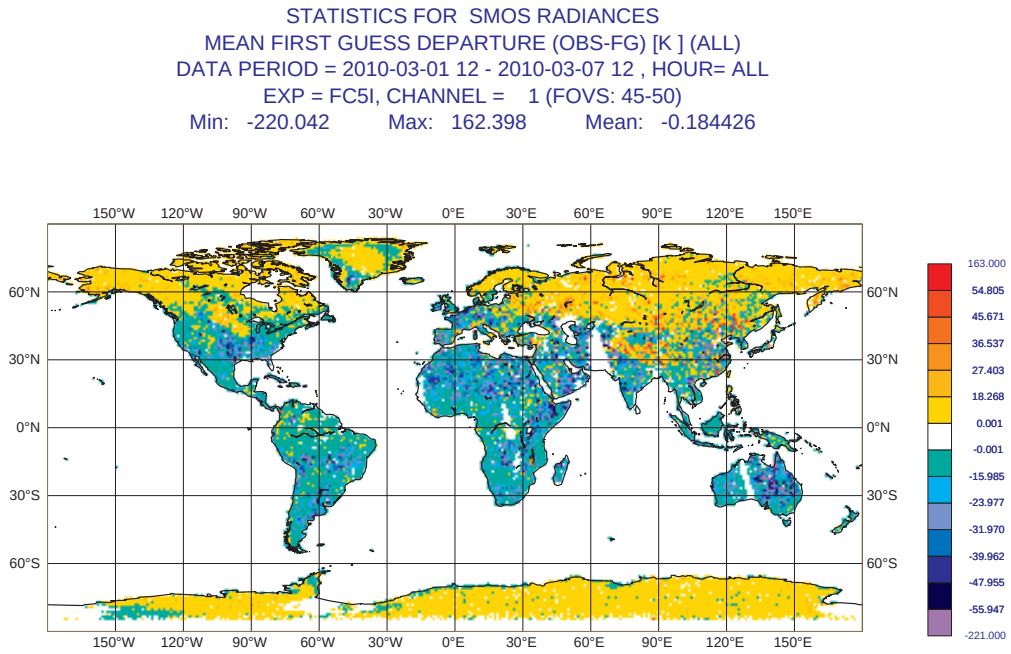

Figure 19: Average of the first-guess departures for the first week of March 2010 at 1 degree spatial resolution. Observations with an incidence angle of 50 degrees and XX polarisation state are only considered in this figure.

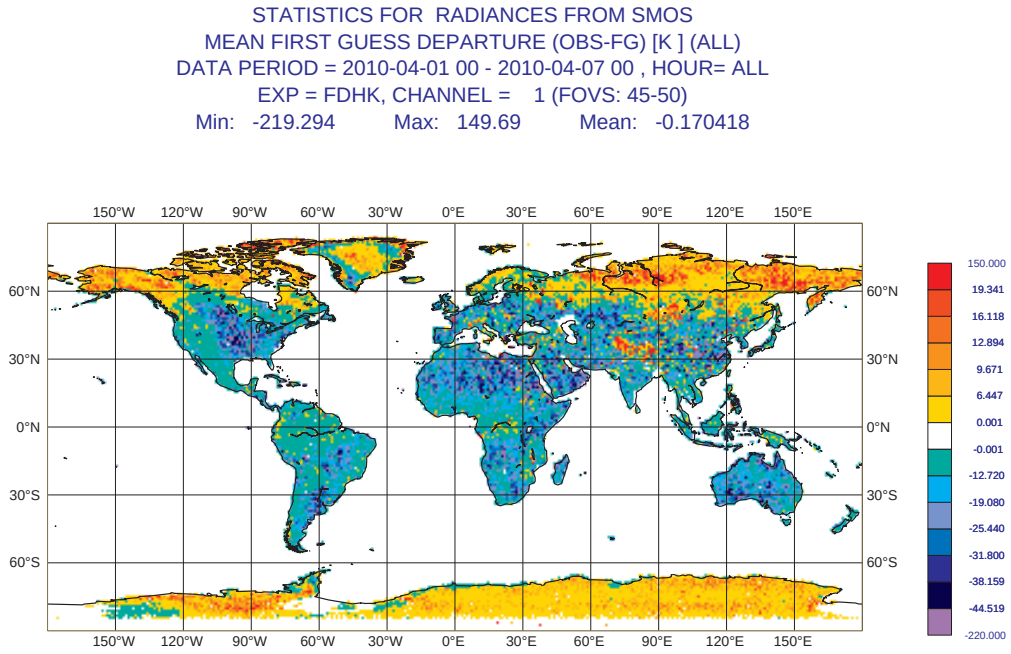

Figure 20: Like Fig. 19, but for the first week of April 2010.

temperatures in L-band to the soil water content, areas presenting high variability could be a sign of strong

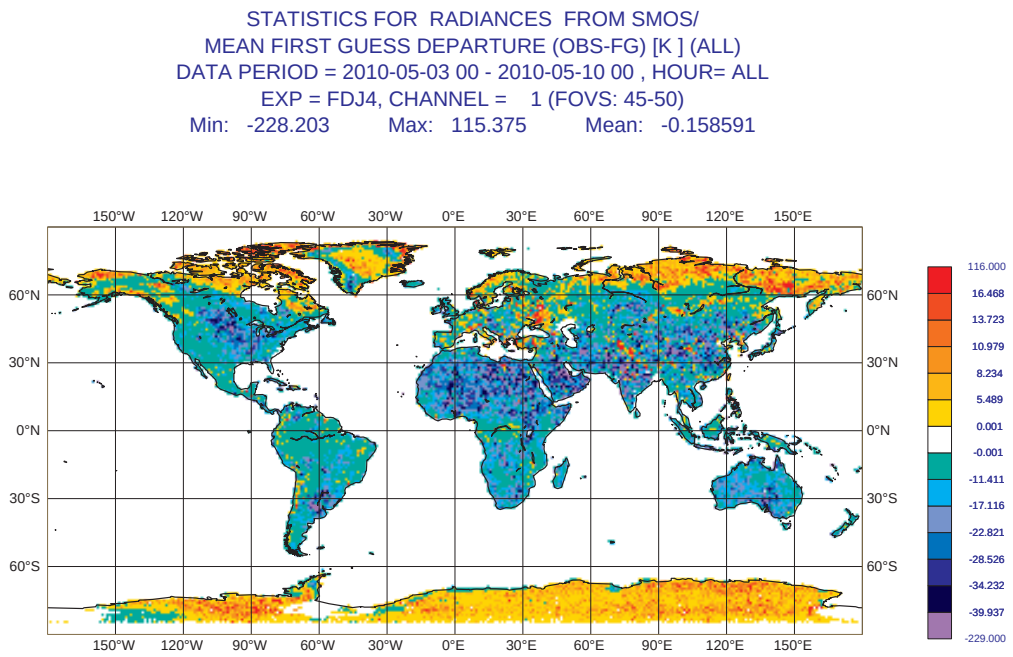

Figure 21: Like Fig. 19, but for the first week of May 2010.

changes in soil moisture and also very interesting areas since the meteorological point of view. However, anomalous large standard deviations might also be a sign that problems in the observations are present. Fig. 22 shows the map of the standard deviation of the SMOS observed brightness temperatures for the first week of March 2010, using only observations with incidence angles between 45 and 50, and for the XX polarisation. Strikingly this figure shows two big red spots covering most of Europe and a good part of the Asian continent. This means that on average over a week all the observations in these areas have a variability larger than 36 K and up to 124 K. This effect cannot be only caused by natural geophysical variability, but is due to the interference by radio frequency emissions in the L-band. Within these zones, strong sources of RFI have been identified. Also areas located hundreds of kms away from the main sources are contaminated and display a significant large unnatural variability.
In Fig. 23 the same statistical variable is computed but for the first week of May. It is worth to mention that the 16^{th} of March 2010 the main source of RFI located in Spain was switched off. This single source was able to contaminate all the way up to the Scandinavian countries in the North of Europe and as far as the North of Africa. By switching off this single source of RFI an extended area of Europe which was previously displaying large values of standard deviation seem now to display more reasonable values, closer to what is expected.

In Fig. 24 only observations for the first week of March 2010 between 55 and 60 degrees are used. The difference with the previous two figures is that it shows the standard deviation of the first-guess departures. This figure shows the variability of the model when compared to the observations. Areas displaying very large anomalous values are, as mentioned, most likely due to RFI, but it also may be an indication of modelling weaknesses under strong variability of the soil conditions.

Fig. 25 shows the standard deviation of the observations for the period from the 5^{th} to the 19^{th} of November 2010 at 40 degrees incidence angle and for the YY polarisation mode. A significant land-sea contamination is

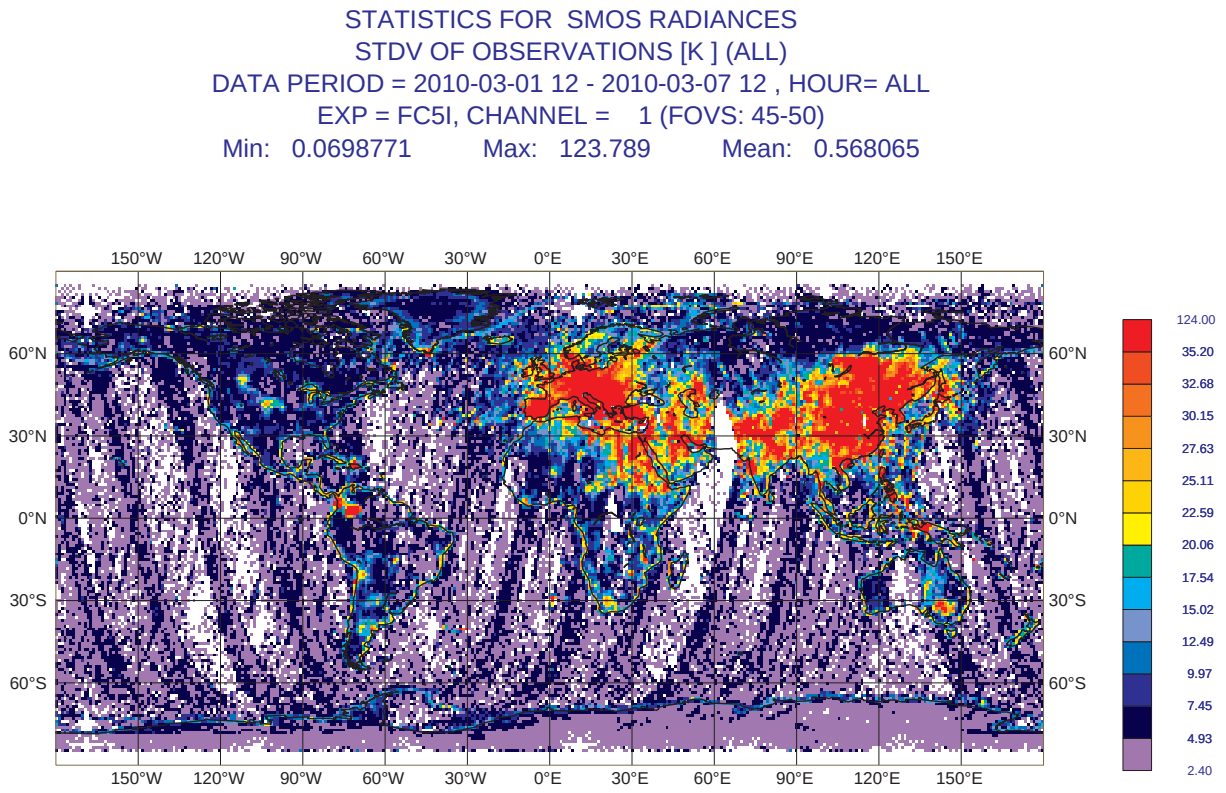

Figure 22: Average of the standard deviation of the SMOS observed brightness temperatures with an incidence angle between 45 and 50 degree for the XX polarisation mode. Values displays correspond to the first week of March 2010.

observed. There is a very large contamination around the European and Asiatic coasts caused by RFI sources over land. As noted earlier, the effect of RFI land sources can reach several hundreds of kms offshore and this effect is sharper with increasing the incidence angle. To a lesser extent, both oceans which surround the North America coasts are contaminated in a well defined band due to a series or military radars located in North America. Other point sources of RFI are also distributed in several locations over the ocean. It is also remarkable to see that the standard deviation of the observations is very elevated in the interface between sea water and sea ice as can be clearly observed for the South Pole. This is coherent with the strong contrast in brightness temperatures between open sea water and water covered by sea ice.

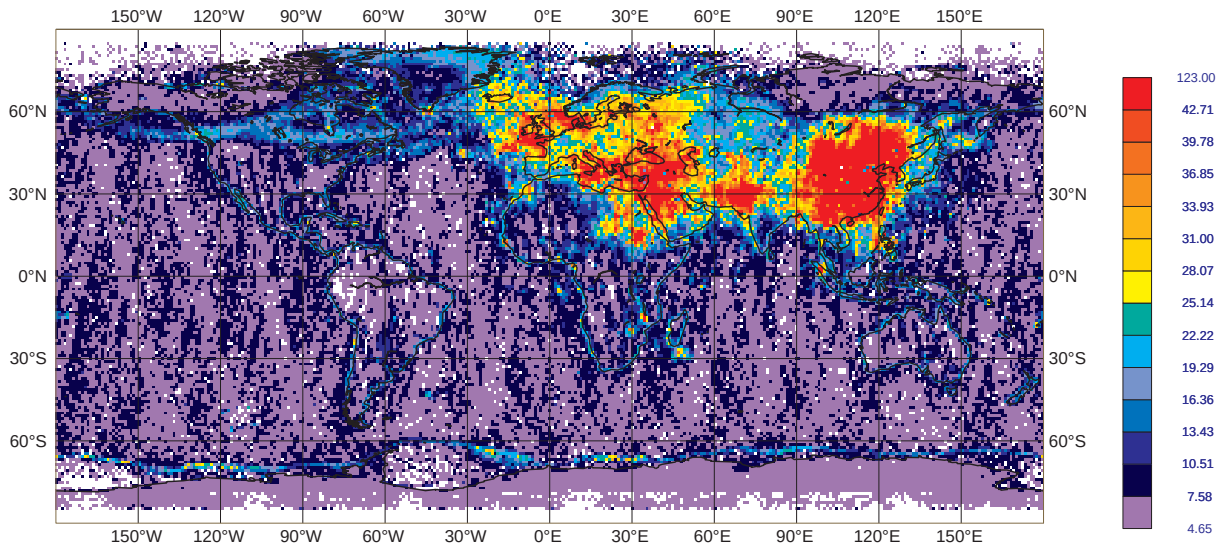

Figure 23: Like Fig. 22, but for 3-10 May 2010.

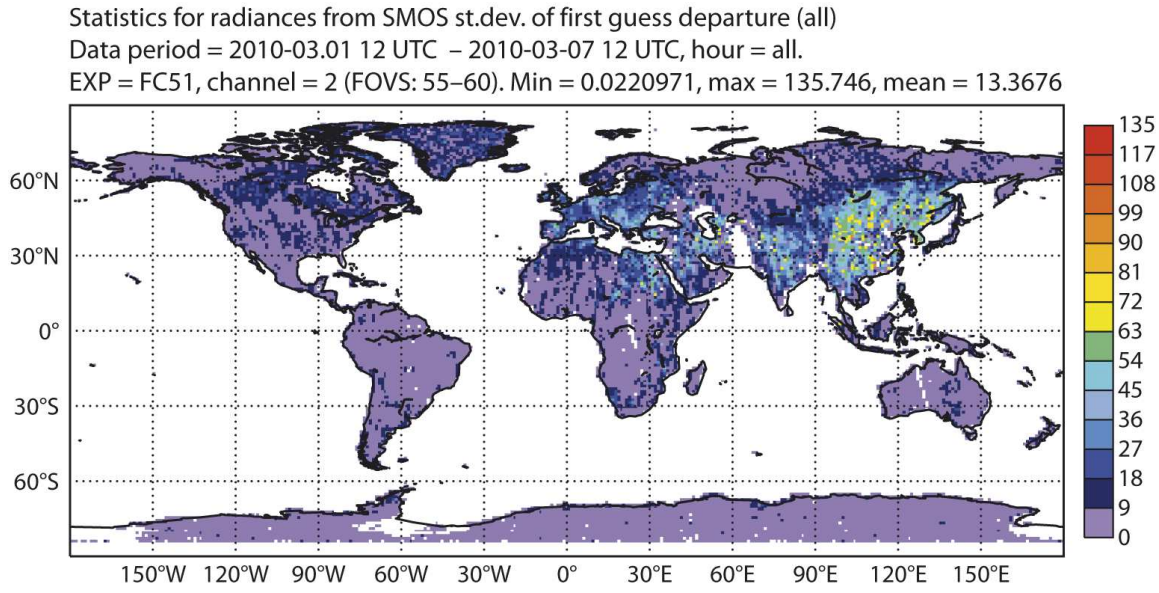

Figure 24: Average of the standard deviation of the differences between SMOS observed brightness temperatures and the brightness temperatures simulated by the CMEM model. Only observations with an incidence angle between 55 and 60 degrees are considered in this figure.

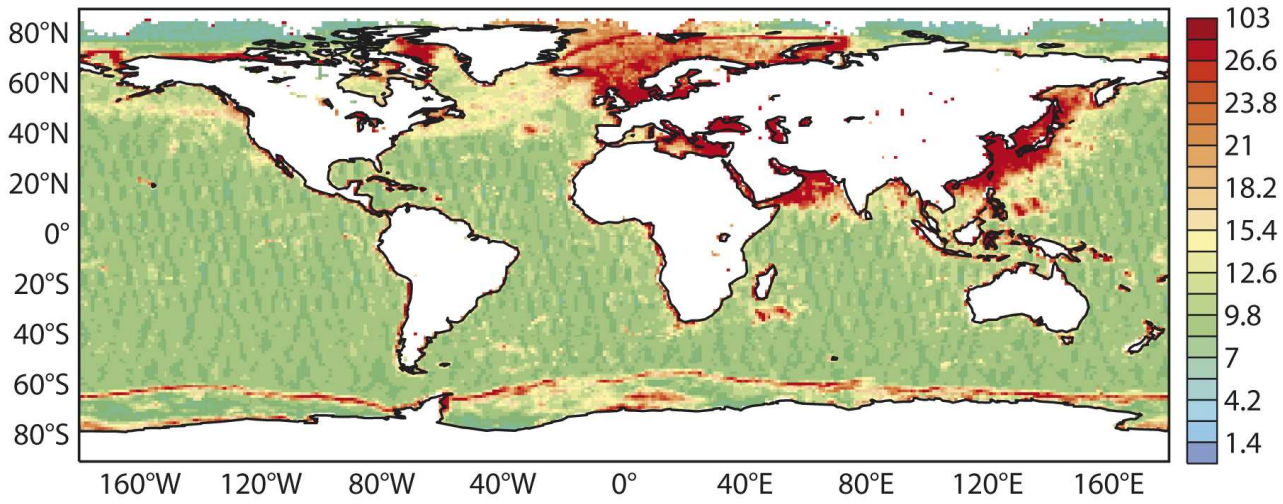

Figure 25: Average of the standard deviation of the SMOS observed brightness temperatures over oceans at 40 degrees incidence angle and for the YY polarisation mode, between the 5^{th} *to the* 19^{th} *of November 2010.*

9 Time series

Time series over long periods at global scale or selected areas provide valuable information about mean bias and trends, but also about possible problems in the observations. Fig. 26 shows time series of averaged statistical variables for continental surfaces at 40 degrees incidence angle and XX polarisation. In the top panel a clear positive trend in the mean bias with time (at least for the displayed period) is observed. A peak in mean bias is apparently due to a problem in the distribution of the data between the 24^{th} and the 26^{th} of November 2010, as shown in the bottom panel. On average the standard deviation of the departures is quite large, being around 29 K. This is basically due to RFI contamination. A daily cycle in observed and modelled brightness temperatures is observed, reflecting the daily cycle of dynamical land variables, in particular soil moisture and soil temperature.

10 Hovmöller plots

Hovmöller plots show one mean-field value averaged per pre-defined bands of latitude as a function of time. These plots make it possible to study to seasonal evolution of average values per latitude bands, as well as localize pointwise temporal problems in the data or in the model. Figs. 27 and 28 show the standard deviation of SMOS observations for the first week of June. Each value displayed in this figure corresponds to a 12 h mean averaged value per 2.5 degrees latitude bands. This figure shows another way to localize the contamination caused by RFI but from a temporal point of view. Red spots in the North Hemisphere can clearly be observed, what means excessive large variability of the observations, in this case produced by RFI. A daily cycle is observed for these red spots with time, this suggests that some of these sources are more active during certain parts of the day. Figs. 27 and 28 show that the observations at XX polarisation mode are more affected by this than in the YY polarisation.

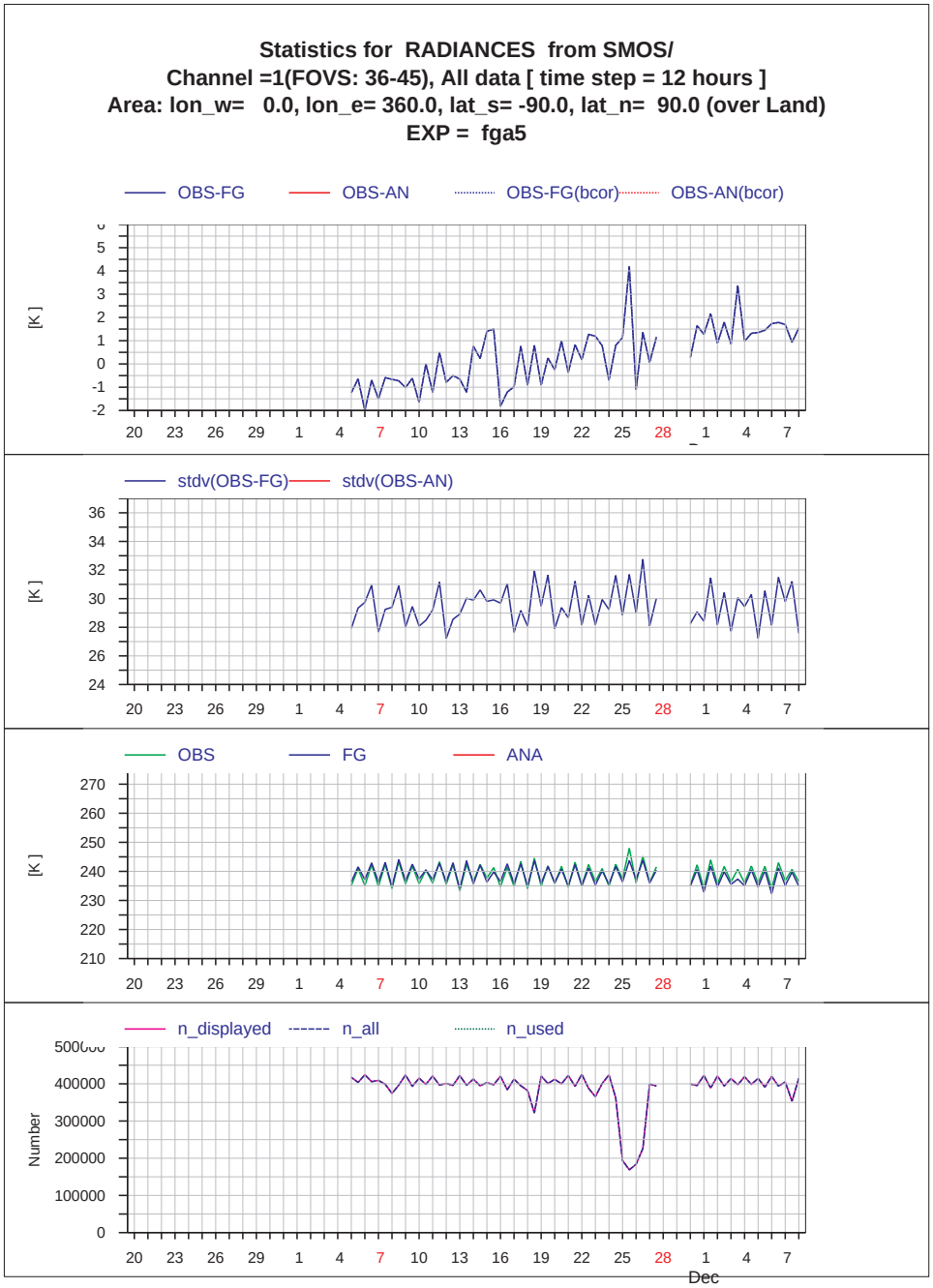

Figure 26: Time series averages of SMOS observed brightness temperatures, simulations by CMEM and departures between both source of data.

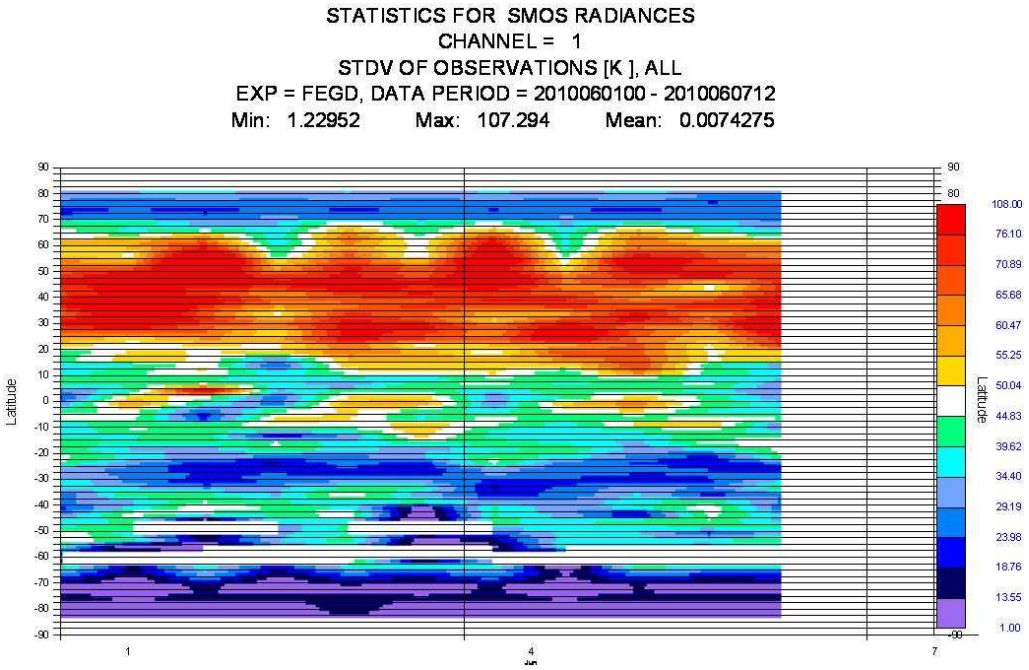

Figure 27: Hovmöeller plot showing the standard deviation of the SMOS observed brightness temperatures for the first week of June 2010 at the XX polarisation mode. The latitudinal resolution is 2.5 degreees.

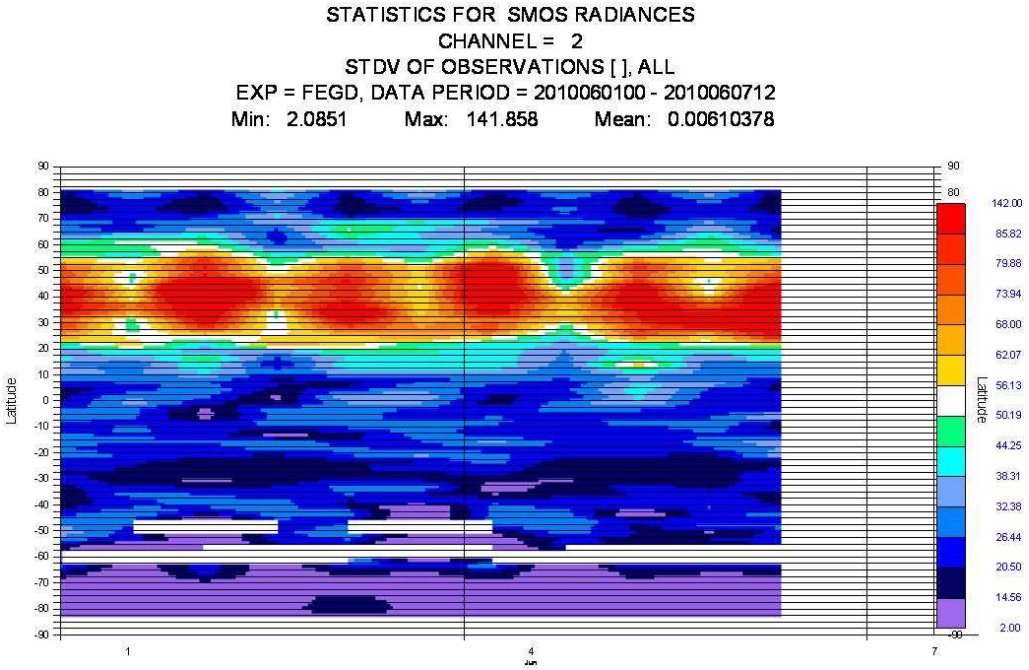

Figure 28: Like Fig. 27, but for the YY polarisation mode.

11 Case study: Pakistan floods

The instrument on-board of the SMOS satellite operates at 1.42 GHz or 21 cm of wavelength. At this wavelength clouds are practically transparent for satellite sensors. Remote sensing sensors in C-band (active or passive) are also sensitive to soil moisture but they are also more sensitive to the cloud liquid water content and integrated water vapour. In contrast the SMOS signal should be very little sensitive to the atmosphere even for adverse weather conditions. Therefore SMOS should have the capability to monitor the soil moisture under conditions where other sensors have problems.
An excellent example of the SMOS observation capabilities is the last week of July 2010, when a large area of Pakistan suffered strong precipitations which caused devastating floods in the area. In this section the spatial correlation between SMOS brightness temperatures and the soil moisture state in Pakistan during July 2010 is investigated. As reference, the soil moisture analysis from ECMWF is used (see Fig. 29). Fig. 30 shows the brightness temperatures observed by SMOS for the period between the 17 and 19 of July 2010. The plot is a composite of three days. This period corresponds to a very dry period in this area, with nul or very small amount of precipitation during the previous weeks. In Fig. 31 the same information is plotted from the 28 to the 30 of July 2010. This is the period when strong precipitations took place and it corresponds to very wet soil. The multi-angular and multi-polarised aspect of the SMOS observations is also represented in these plots. Observations are plotted only at the following incidence angles: 10, 20, 30, 40, 50 and 60, with a margin of 0.5 degrees. This margin has been found to be optimal to investigate the correlation between SMOS brightness temperatures and the soil water content of the top soil layer. A smaller margin produces big gaps in these figures, as a very reduced number of observations is selected, whereas a larger margin produces undesired effects (too much overlapping between different orbits and spread of contamination by use of the extended alias free field of view (EAFOV)). Observations without physical meaning are filtered out (greater than 340 K or lower than 100 K). Soft RFI could still be embedded in the remaining signal.
These figures show the following:

- The scene is completely covered by observations with incidence angles of 40 degrees of larger. Observations with incidence angles of 20 or 30 degrees are quite affected by the extended alias free field of view (EAFOV) as for these angles most of the observations are within the EAFOV. In particular the edge of the satellite track displays very different brightness temperatures values. As the incidence angle increases more observations are obtained in the alias free area, thus increasing the quality of the observations.
- Either for the dry set or the wet set, the SMOS signal behaves as expected theoretically, i.e., brightness temperatures getting warmer with increasing the incidence angle for the YY polarisation, whereas they get colder with increasing incidence angle for the XX polarisation mode.
- There is a substantial and clear difference in brightness temperatures between the dry and wet conditions. Brightness temperatures are in all cases clearly colder for the wet conditions as it should be.
- Figures with an incidence angles of 50 and 60 are the most informative ones (most of the observations in the alias free area, covers the whole area, lower effect of the satellite edge).
- For the dry set, it is observed that in general the western part of the geographical area displayed is slightly drier than the East part. This is consistent with the soil moisture state of this period, however the figure is very patchy and a clear correlation is not observed. The slope of the terrain in the area and the roughness effect for dry soil could be a possible cause.
- For the wet set, for 50 degrees and 60 degrees incidence angle a good correlation is observed with the ECMWF soil moisture analysis. This is clearly observed at 50 degrees for the H-pol, displaying very cold and contrasting brightness temperatures for the flooded area in Pakistan. A drier patch is also observed on the border with India, which correlates very well with the ECMWF soil moisture analysis.

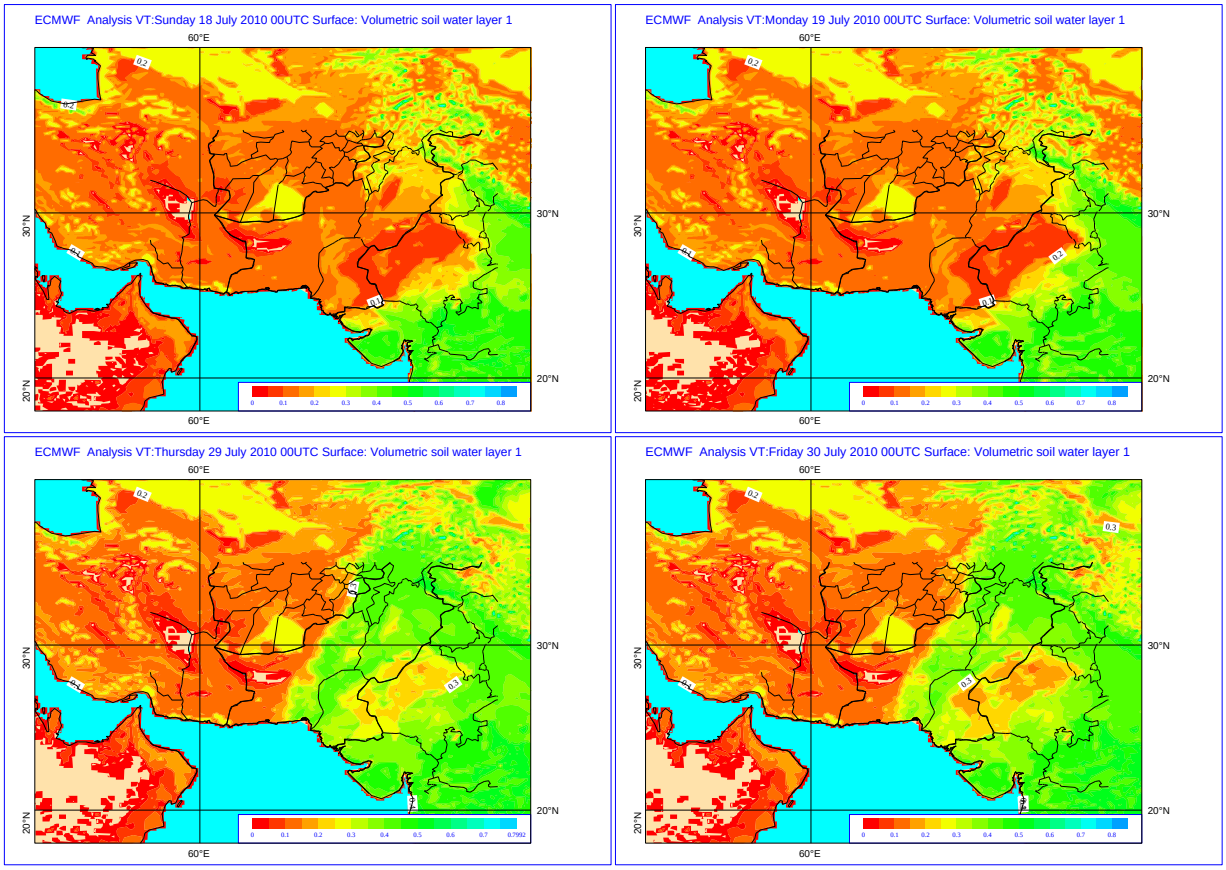

Figure 29: ECMWF soil moisture analysis for the top soil layer (7cm). Units are in m^3/m^3 volumetric soil moisture fraction. Top left corresponds to the 18^{th} of July 2010, Top right 19^{th} of July 2010, bottom left 29^{th} of July 2010 and bottom right 30^{th} of July 2010.

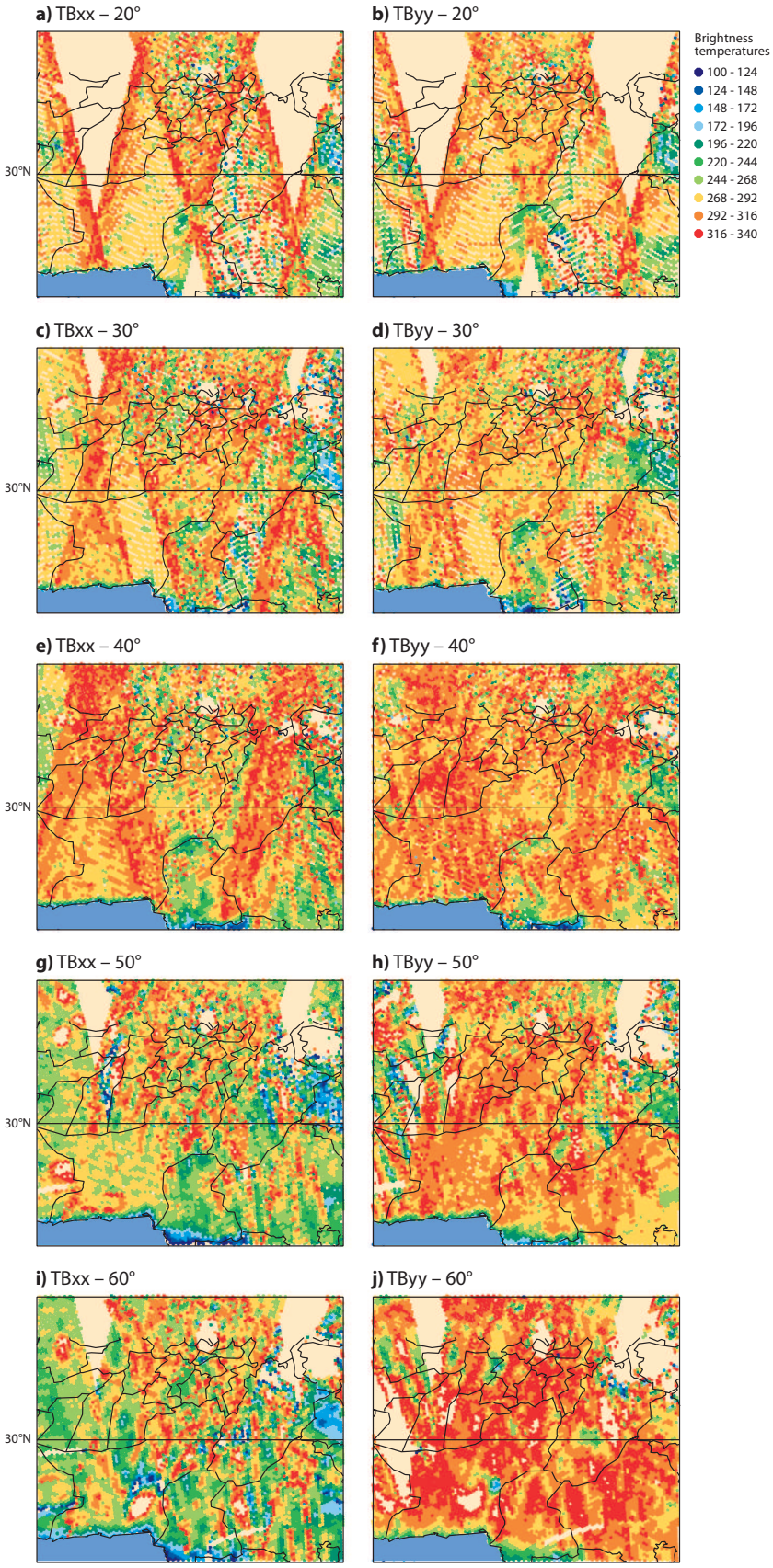

Figure 30: Brightness temperatures as seen by SMOS for the Pakistan area, between the 17th and the 19th of July 2010. Left column corresponds to XX polarisation, right column to the YY polarisation.

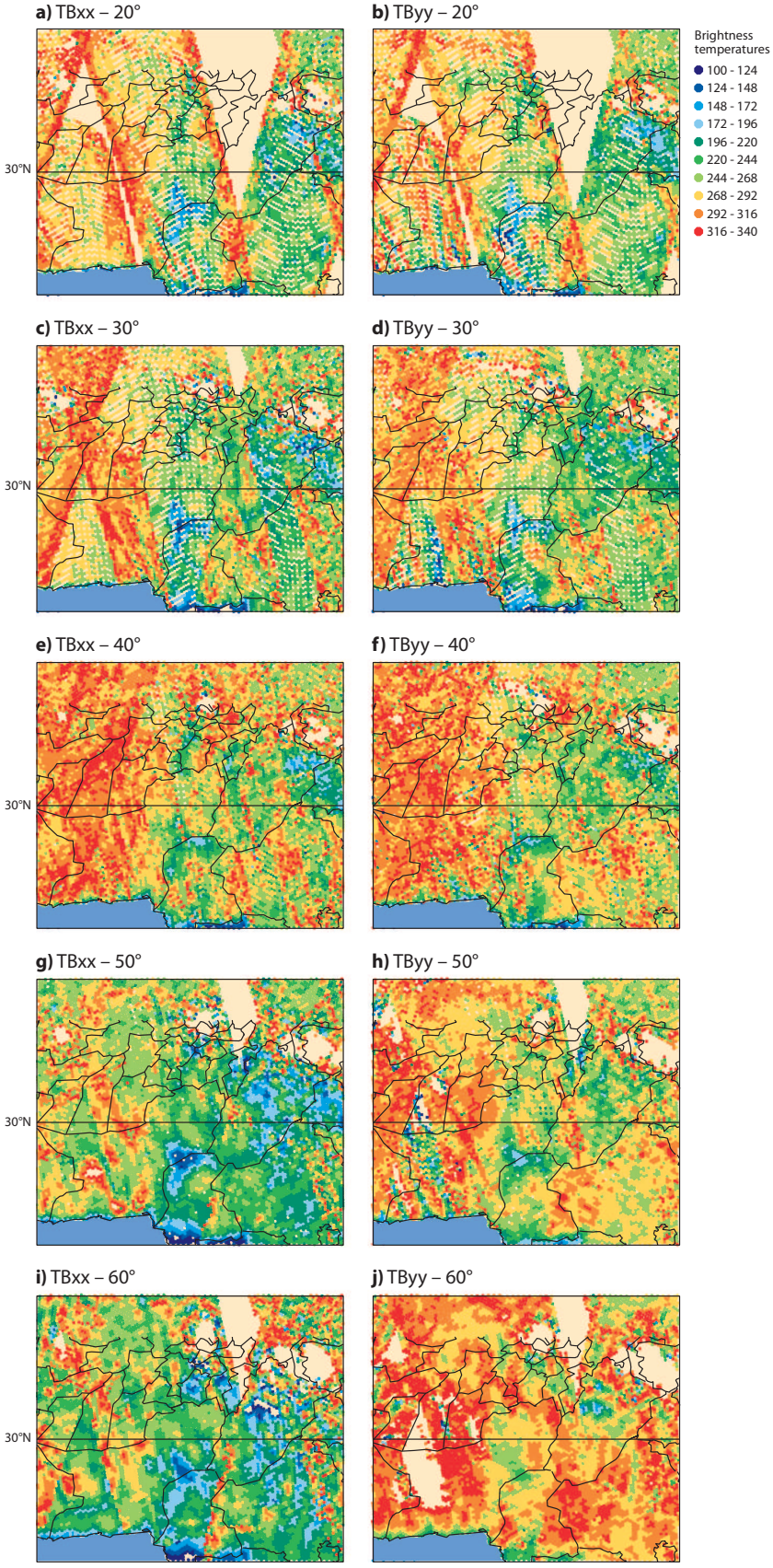

Figure 31: Like Fig. 30, but for the period between the 28th to the 30th of July 2010.

12 Summary and Conclusions

This first Report of a series of SMOS monitoring reports is intended to describe the sort of statistical products which are routinely produced at ECMWF with SMOS data, and demonstrate the potential of SMOS observations to monitor the surface state and in particular, the soil moisture state.

The ECMWF passive microwaves emission model CMEM is used to simulate brightness temperatures at the top of the atmosphere. Geolocated SMOS observed brightness are compared to CMEM outputs at the satellite antenna reference frame and in near real time, producing first guess departures. The analysis of the source of first guess departures has demonstrated that Radio Frequency Interference (RFI) is the main source producing strong disagreements with the modelled brightness temperatures, either producing a strong dry or a wet bias. However, mountainous regions and coastlines also produce very large departures. To a lesser extent, snow, ice, boreal forests and rough dry surfaces at large incidence angles show large departure due to the lack of a good modelling in passive L-band with the current parameterizations of the forward model. The comparison of histograms of first-guess departures between the current cycle (cycle 36r4) and an old one (cycle 36r1) has demonstrated that large differences with the observations have been reduced. The cause is twofold, on the one hand recent calibrations of the instrument have improved the quality of the observations, on the other hand the improved model physics used in the current cycle has also improved the CMEM model equivalents.

Time-averaged geographical field means reflect the average state of the surface. The first results show that for both simulated polarisation and except for areas affected by RFI, brightness temperatures behave as expected. An excellent correlation between sea ice extent maps and time averaged SMOS brightness temperatures is found.
First-guess departures show a good correlation with snow covered areas, and in particular the snow line can be monitored with first guess departures mean values.
Plots of the standard deviation of the observed brightness temperatures and of the first-guess departures show pixels which are very sensitive to RFI contamination. Combining both sources of information could be a good resource to discriminate between RFI or signal due to high variability of the geophysical variables. Also large variability is found in the interface between sea ice and sea water.
Hovmöller plots can be combined with geographical mean fields to localize temporal problems in the data or in the model. They are also useful to evaluate the latitudinal effect of RFI in the L-band signal. Time series plots make it possible to monitor mean bias trends. Soon the SMOS monitoring web page will offer the possibility of obtaining the statistics for selected areas.

In the monitoring reports which will follow this one, reports based on long-term statistics starting from November 2010 will be presented.

Acknowledgements

This work is funded under the ESA-ESRIN contract number 20244/07/I-LG and is Part 1 (MR1) of a series of Monitoring Reports to ESA. The authors would like to thank Milan Dragosavac and Ioannis Mallas for the operational acquisition and contribution to the processing of the data, Anna Fouilloux for her help with the technical implementation, and Lars Isaksen for his useful advice.

References

[Balsamo et al. 2009] Balsamo, G., P. Viterbo, A. Beljaars, B. van den Hurk, M. Hirschi, A. Betts, and K. Scipal, 2009 : A revised hydrology for the ECMWF model: Verification from field site to terrestrial water storage and impact in the integrated forecast system. *Journal of Hydrometeorology*, **10**,623–643. doi: 10.1175/2008JHM1068.1.

[Choudhury et al. 1979] Choudhury, B. J., T. J. Schmugge, A. Chang, and R. W. Newton, 1979 : Effect of surface roughness on the microwave emission for soils. *Journal of Geophysical Research*, **84**,5699–5706.

[de Rosnay et al. 2009a] de Rosnay, P., M. Drusch, A. Boone, G. Balsamo, B. Decharme, P. Harris, Y. Kerr, T. Pellarin, J. Polcher, and J.-P. Wigneron, 2009a : AMMA Land Surface Model Intercomparison Experiment coupled to the Community Microwave Emission Model: ALMIP-MEM. *J. Geophys. Res.*, **114**. D05108, doi:10.1029/2008JD010724.

[de Rosnay et al. 2009b] de Rosnay, P., M. Drusch, and J.M. Sabater, 2009b : Milestone 1 Technical Note Part I: SMOS global surface emission model. Technical report, European Centre for Medium-Range Weather Forecast, Reading, United Kingdom.

[Drusch et al. 2001] Drusch, M., T. Holmes, P. de Rosnay, and G. Balsamo, 2001 : Vegetative and atmospheric corrections for the soil moisture retrieval from passive microwave remote sensing data: Results from the southern great plains hydrology experiment 1997. *J. Hydrometeor.*, **2**,181–192.

[Drusch et al. 2009] Drusch, M., T. Holmes, P. de Rosnay, and G. Balsamo, 2009 : Comparing ERA-40 based L-band brightness temperatures with Skylab observations: A calibration / validation study using the Community Microwave Emission Model. *Journal of Hydrometeorology*, **10**,213–226. doi: 10.1175/2008JHM964.1.

[Holmes et al. 2008] Holmes, T., M. Drusch, J.-P. Wigneron, and R. de Jeu, 2008 : A global simulation of microwave emission: Error structures based on output from ECMWFS operational integrated forecast system. *IEEE Transactions on Geoscience and Remote Sensing*, **46**,846 – 856.

[Kirdyashev et al. 1979] Kirdyashev, K., A. Chukhlantsev, and A. Shutko, 1979 : Microwave radiation of the earth's surface in the presence of vegetation cover. *Radiotekhnika i Elektronika*, **24**,256–264.

[Matos and Gutierrez 2004] Matos, P., and A. Gutierrez, 2004 : SMOS L1 processor discrete global grids document. Technical report, Deimos Engenharia, Lisboa, Portugal.

[Pellarin et al. 2003] Pellarin, T., J.-P. Wigneron, J.-C. Calvet, and P. Waldteufel, 2003 : Global soil moisture retrieval from a synthetic l-band brightness temperature data set. *Journal of Geophysical Research*, **108**.

[Sabater et al. 2010a] Sabater, J.M., P. de Rosnay, and A. Fouilloux, 2010a : Milestone 2 Technical Note, Part I:operational pre-processing chain, Part II:collocation software development, Part III: Offline monitoring suite. Technical report, European Centre for Medium-Range Weather Forecasts, Reading, United Kingdom.

[Sabater et al. 2010b] Sabater, J.M., P. de Rosnay, and G.Balsamo, 2010b : Sensitivity of L-band NWP forward modelling to soil roughness. *Int. J. Remote Sens.* doi: 10.1080/01431161.2010.507260. In press.

[Salgado 1999] Salgado, R., 1999 : Global soil maps of sand and clay fractions and of the soil depth for MESONH simulation based on FAO/UNESCO soil maps. Technical report, CNRM/Météo France. Tech. Note, **59**.

[Wang and Schmugge 1980] Wang, J. R., and T. Schmugge, 1980 : An empirical model for the complex dielectric permittivity of soils as a function of water content. *IEEE Transactions on Geoscience and Remote Sensing*, **18**,288–295.

[Wigneron et al. 2007] Wigneron, J.-P., Y. Kerr, P. Waldteufel, K. Saleh, M.-J. Escorihuela, P. Richaume, P. Ferrazzoli, P. de Rosnay, R. Gurneye, J.-C. Calvet, J. Grant, M. Guglielmetti, B. Hornbuckle, C. Mtzler, T. Pellarin, and M. Schwank, 2007 : L-band microwave emission of the biosphere (L-MEB) model: Description and calibration against experimental data sets over crop fields. *Remote Sensing of Environment*, **107**,639–655.

[Wigneron et al. 2001] Wigneron, J. P., L. Laguerre, and Y. Kerr, 2001 : A simple parameterization of the L-band microwave emission from rough agricultural soils. *IEEE Transactions on Geoscience and Remote Sensing*, **39**,1697–1707.